

# Generative Structural Design

## Integrating BIM and Diffusion Model

Zhili He<sup>a</sup>, Yu-Hsing Wang<sup>a\*</sup>, Jian Zhang<sup>b</sup>

<sup>a</sup>*Department of Civil and Environmental Engineering,*

*The Hong Kong University of Science and Technology, HKSAR, China*

<sup>b</sup>*School of Civil Engineering, Southeast University, Nanjing, China*

### ABSTRACT:

Intelligent structural design using AI can effectively reduce time overhead and increase efficiency. It has great potential to become the new design paradigm in the future to assist and even replace human engineers, and therefore it has become a research hotspot in the academic community. However, current methods have some limitations to be addressed urgently, whether in terms of application scope, visual quality of generated results, or evaluation metrics of results. This study proposes a comprehensive solution. Firstly, this paper introduces building information modeling (BIM) into intelligent structural design and establishes a structural design pipeline integrating BIM and generative AI, which is a powerful supplement to the previous frameworks that only considered CAD drawings. In order to improve the perceptual quality and details of generations, this study makes 3 contributions. Firstly, in terms of generation framework, inspired by the process of human drawing, a novel 2-stage generation framework is proposed to replace the traditional end-to-end framework to reduce the generation difficulty for AI models. Secondly, in terms of generative AI tools adopted, diffusion models (DMs) are introduced to replace widely used generative adversarial network (GAN)-based models, and a novel physics-based conditional diffusion model (PCDM) is proposed to consider different design prerequisites. Thirdly, in terms of neural networks, an attention block (AB) consisting of a self-attention block (SAB) and a parallel cross-attention block (PCAB) is designed to facilitate cross-domain data fusion, *i.e.*, image data and condition data. Then, in order to evaluate the generated design drawing comprehensively, a subjective metric consistent with human perception is further introduced. The quantitative and qualitative experimental results demonstrate the powerful generation and representation capabilities of PCDM. Necessary ablation studies are conducted to further examine the validity of the proposed methods. This study also shows that DMs have the potential to replace GANs and become the new benchmark for generative problems related to civil engineering.

### Keywords:

Generative AI, Diffusion Model, Building information modeling, Intelligent structural design, Shear wall structure

## 1. Introduction

In the entire lifecycle of building projects, the structural design of buildings is one of the most crucial and indispensable tasks. With the acceleration of global urbanization, a huge number of buildings are designed and constructed every year [1], which also brings a heavy and increasing demand in terms of structural designs.

Currently, structural designs are completed by structural engineers. This manual work has two prominent features. Firstly, structural designs rely heavily on immense structural knowledge and design experience [2], which

---

\* Corresponding author.

E-mail addresses: [ceyhwang@ust.hk](mailto:ceyhwang@ust.hk) (Y.-H. Wang).

makes it almost impossible for humans to consider all explicit and implicit rules and constraints [3]. Therefore, this leads to the second characteristic: structural designs cannot be completed in one go, and their nature is continuous repetition and iteration. Thus, structural designs are always time-consuming [1], labor-intensive, and inefficient [4], making it difficult to meet the current heavy demands [2] so that as everyone knows, overtime is quite common in design institutes. Practitioners urgently need an innovative and intelligent design paradigm to alleviate the above issues.

Nowadays, the rapidly evolving and widely followed AI technologies are bringing revolutionary solutions to many industries [5][6]. Current AI technologies based on a data-driven paradigm [7] have 2 outstanding features. First, AI models are trained on big data to learn, remember, and represent massive data characteristics. Compared to humans, AI models have “infinite” memory; namely, the richer the data, the stronger the performance and representation ability that model can theoretically achieve. For example, large language models, such as ChatGPT and GPT-4, are trained on a massive human knowledge base and even have unpredictable emergent abilities [8]. Second, the AI models are automated and efficient, and their inference time can be negligible. Combining the 2 characteristic of structural design, AI models are naturally suitable for structural design tasks and have great potential to become the new structural design paradigm in the future. Therefore, at this stage, how to integrate AI and structural designs has become a research hotspot in the academic community.

Further, the forms and layouts of buildings are very diverse, and at the current fledgling research stage, it is unrealistic to consider all types of buildings in AI models. Because on the one hand, high-rise residential buildings adopting reinforced concrete shear wall systems are the primary high-rise building type among numerous buildings and occupies a significant proportion [1][9], and the design and construction demand is continuously increasing [10] due to the rapid increase in global population (there is a heavy and increasing design demand and rich design data), and on the other hand, the layout of this type of buildings is very regular, for example, rooms are almost all rectangular in shape, and structural configuration consists of a few rectangular walls [11][12] (there is strong regularity in design to make it easier for AI to design), current research focus of academic community is intelligent designs of shear wall residential buildings using AI [1][2][3][11][12]. Specifically, these studies can be divided into two categories, namely, regression-based methods and generative model-based methods, and they are detailed below.

**Regression-based methods.** Pizarro et al. [11][12] were the first group of people to start this study, and they trained multi-layer perceptrons (MLPs) and convolutional neural networks (CNNs) to directly design the layout of shear wall structures using pixel-level regression loss functions (the most widely adopted functions are  $L_1$  or  $L_2$  loss functions) in a supervised learning and end-to-end way. However, suffering from the limited representation power of the end-to-end regression-based methods in image synthesis tasks, their generation results are relatively rough. Specifically, the limited representation power is reflected in 3 aspects: (1) These end-to-end regression-based methods are committed to optimizing popular distortion-based metrics, but distortion-based metrics and human perceptual quality are at odds with each other [13], and images reconstructed by the algorithms picked by the metrics often have visibly lower quality [14]. (2) Regression-based methods are prone to recovering images with fewer high-fidelity details [15], since the regression losses are conservative with high-frequency details [16]. (3) The goal of regression-based methods is to directly fit the training set, so the diversity of generated results and generalization ability of models are insufficient. Zhao et al. [4][18] introduced graph neural networks (GNNs) [17] to innovate the end-to-end regression-based method. They first convert the original architecture layout into a graph representation and then train GNN models by minimizing regression loss functions between GNN-generated shear wall layout designs and ground-truths. In the inference stage, they generate shear wall designs using a trained GNN with a reverse graph representation. This kind of indirect regression-based method incorporates prior graph constraints so that it can generate more precise design drawings than traditional end-to-end regression-based methods. However, it still suffers from the inherent disadvantage of regression-based methods, namely, a lack of diversity. Besides,

graph representation is a bit cumbersome.

**Generative model-based methods.** Then, another solution has emerged, *i.e.*, deep generative models. Unlike regression-based methods directly fitting datasets, generative model-based methods first learn and model complex data distributions of images and then generate high-quality samples based on the learned distributions. Extensive research has shown that more detailed, diversified, convincing, and perceptually plausible images can be generated using deep generative models [14][15][16][19]. Therefore, this paper’s solution is designed based on deep generative models. Deep generative models can usually be divided into 2 categories: (1) likelihood-based methods, such as variational autoencoders (VAEs) [20], flow-based generative models [21][22], and autoregressive models [23]. (2) adversarial training-based models, *i.e.*, generative adversarial networks (GANs) [24]. As a representative method of deep generative models, GAN is born for better image generation, and extensive research has shown GANs exhibit higher and more refined sample quality than likelihood-based methods [19][25]. Therefore, GANs have been widely used on most computer vision tasks, such as style transfer [26] and image restoration [27][28]. In the field of civil engineering, GANs also have many successful applications, such as bolt inspection [29], crack segmentation [30][31], and house floorplan generation [32][33][34]. Inspired by the successes, Liao et al. [1] extended the application of GAN to the intelligent design of shear walls to propose StructGAN [1] and a series of variants, such as StructGAN-PHY [2] and StructGAN-AE [3]. These studies have drawn extensive attention and become the most representative research progress in this field. However, this paper holds that there are still 4 points worth further studying and improving, which are introduced below.

The first aspect is the application scope. All the StructGAN-based models are built based on CAD design drawings [2]. In fact, building information modeling (BIM) technology has been widely used throughout the entire lifecycle of buildings [35] to facilitate information management, raise efficiency, increase transparency, etc. Besides, BIM is even mandatory for some countries or regions, such as Hong Kong, where capital works projects with project estimates of more than 30 million HKD must use BIM technology [36]. Hence, this paper extends the BIM application to the shear wall intelligent design and proposes a structural design pipeline combining BIM and generative AI, denoted as **generative BIM** for simplicity, as presented in Section 2.

The second aspect is the adopted generation framework. The StructGAN-based methods are all end-to-end generative model-based methods; namely, input images are architectural design drawings, and the generation framework wants AI models to predict structural design drawings directly, which means AI models should first understand the architectural drawings and then “*draw*” key objects (*i.e.*, shear walls) on semi-finished paintings (*i.e.*, architectural design drawings) without changing any other parts. Obviously, the generating tasks are a little hard to handle, and as shown in Fig. 1 (a), there is still room for improvement in the generation results of StructGAN in perceptual quality and details. Because we have found a latent relationship between generation tasks and drawing, this paper considers this generation problem from another perspective. Inspired by the human drawing process, this study designs a 2-stage generation framework to simplify the generation tasks, where AI models’ task is changed to paint a line drawing based on a given canvas. Details are given in Section 3.

The third aspect is the deep generative model and the network structure used. The visual quality of the StructGAN’s generation images is also limited by the adopted GANs besides the generation framework. Specifically, the adversarial training nature of GANs mainly brings two problems: (1) Training is unstable and oscillating, and in order to stabilize training, GAN models require carefully designed choices and tricks in optimization and structures [37], *e.g.*, a fancy model, pix2pixHD [38], is selected as the basic model of StructGAN. (2) They fail to explore and cover the whole distribution of training data [39]. In other words, GANs become stuck in some particular modes of true data distribution while ignoring many other useful modes, even if the missing modes are present throughout the data [40], *i.e.*, the notorious problem of **mode collapse**. For example, as shown in Fig. 1 (a), the part of the boundaries of the designed walls doesn’t meet the basic design requirement, namely, boundaries

should preferably be horizontal or vertical. Besides, generation results are not clear enough. These all mean that many key modes of data are not covered. Therefore, a large amount of post-processing work is inevitable. Fortunately, a novel likelihood-based generative model without adversarial training, diffusion models (DMs) [41], represented by the denoising diffusion probabilistic model (DDPM) [42], has been proposed recently and has attracted extensive attention from researchers. Research shows that DMs are capable of modeling arbitrarily complex image distributions and have achieved impressive and state-of-the-art (SOTA) results not only in the field of image synthesis [43][44], but also in nearly all downstream computer vision tasks, such as image restoration, including super-resolution [15], image deblurring [14][16], inpainting [45], denoising [46], deraining [47], etc. However, whether DMs are competent for the design task of shear walls is still unknown. This paper makes some explorations and proposes a physics-based conditional diffusion model (PCDM). Compared with the traditional DMs, on the one hand, PCDM predicts the original clean image rather than noise, and Section 4 analyzes the theoretical equivalence and actual effectiveness in ensuring the design similarity. On the other hand, PCDM embeds physical conditions to consider the design differences among shear wall drawings. In order to facilitate cross-domain data fusion (*i.e.*, drawing data and condition data), a novel attention block (AB) consisting of a self-attention block (SAB) and a parallel cross-attention block (PCAB) is designed and plugged into the neural network. PCDM is expounded in Section 4.

The fourth aspect is the evaluation metrics adopted. StructGAN and its variants only use the objective metric, which is calculated by pixel-level comparing predicted results with labels. Subjective metrics that can quantitatively evaluate the visual quality of generated samples by simulating human perception are neglected. Therefore, this study further introduces a subjective metric (see Section 5) to judge if the generated drawings *look like* the structural design drawings designed by engineers. Combining both kinds of metrics can result in a more comprehensive evaluation of performance.

Fig. 1 (b) gives an example to show the effectiveness of the designed generation framework based on PCDM, which learns design experiences from design data and models the true image distribution correctly. More experimental results are presented in Section 6 and further validate the powerful generation and representation capabilities of the proposed method.

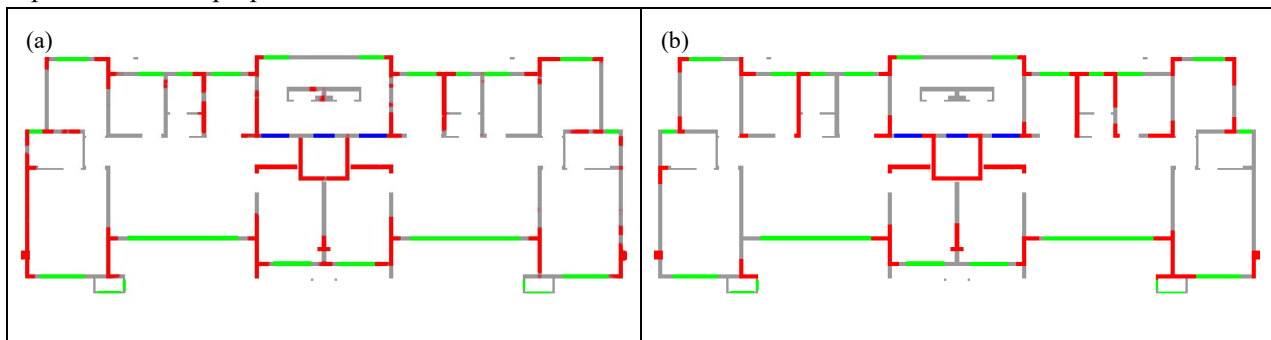


**Fig. 1.** The overall framework of the structural design pipeline based on BIM and AI: (a) The result of StructGAN, (b) The result of PCDM. The red pixels denote shear walls, and the grey pixels represent infill walls. The more detailed explanation is listed in Section 3.

In short, the main contributions of this study are:

- (1) Application scope. This paper extends the BIM application to shear wall intelligent design and proposes a generative BIM structural design framework.
- (2) Generation framework. End-to-end generative model-based methods are extended to the indirect generative model-based method. Inspired by the human drawing process, a 2-stage generation framework is designed.
- (3) Generative model. This paper extends the DM application to shear wall intelligent generation and develops a

modified DM, PCDM. Regarding the change in predicting objects, this paper demonstrates the equivalence from the theoretical perspective and the effectiveness from the practical perspective. To the authors' best knowledge, this is the first work to systematically research the integration of DMs and civil engineering, and DMs has the potential to become the new benchmark in the generative problems of civil engineering. Because there is a little math in DMs, this paper revolves around the core idea of DMs and strives for an intuitive and succinct explanation to facilitate civil engineering community understanding. Strict theoretical derivation and proof are provided in the appendix.

- (4) Network structure. In order to facilitate cross-domain data fusion, an attention block (AB) consisting of a self-attention block (SAB) and a parallel cross-attention block (PCAB) is designed and plugged into the network.
- (5) Evaluation metric. The subjective metric is introduced to obtain a more accurate and synthetic evaluation of the models' performance together with the objective metric.

The paper is organized in the following way: First, Section 2 expounds on the proposed structural design pipeline based on generative BIM. Detailed descriptions of the 2-stage generation framework are presented in Section 3. Section 4 details the designed PCDM and the attention block. The implementation details of the methods are described in Section 5. In Section 6, experimental results and discussion are presented in detail. Finally, Section 7 provides conclusions and future work. The implementation code of the generative BIM, the code of PCDM, and the dataset used are all available at <https://github.com/hzlbfbrog/Generative-BIM>.

## 2. Proposed generative BIM structural design pipeline

The automatic and intelligent structural design pipeline based on generative BIM is illustrated in Fig. 2, which includes four stages: (1) standardization: from BIM; (2) intelligent structural design; (3) standardization: to BIM; and (4) integrated BIM. This section is going to introduce this proposed framework in detail.

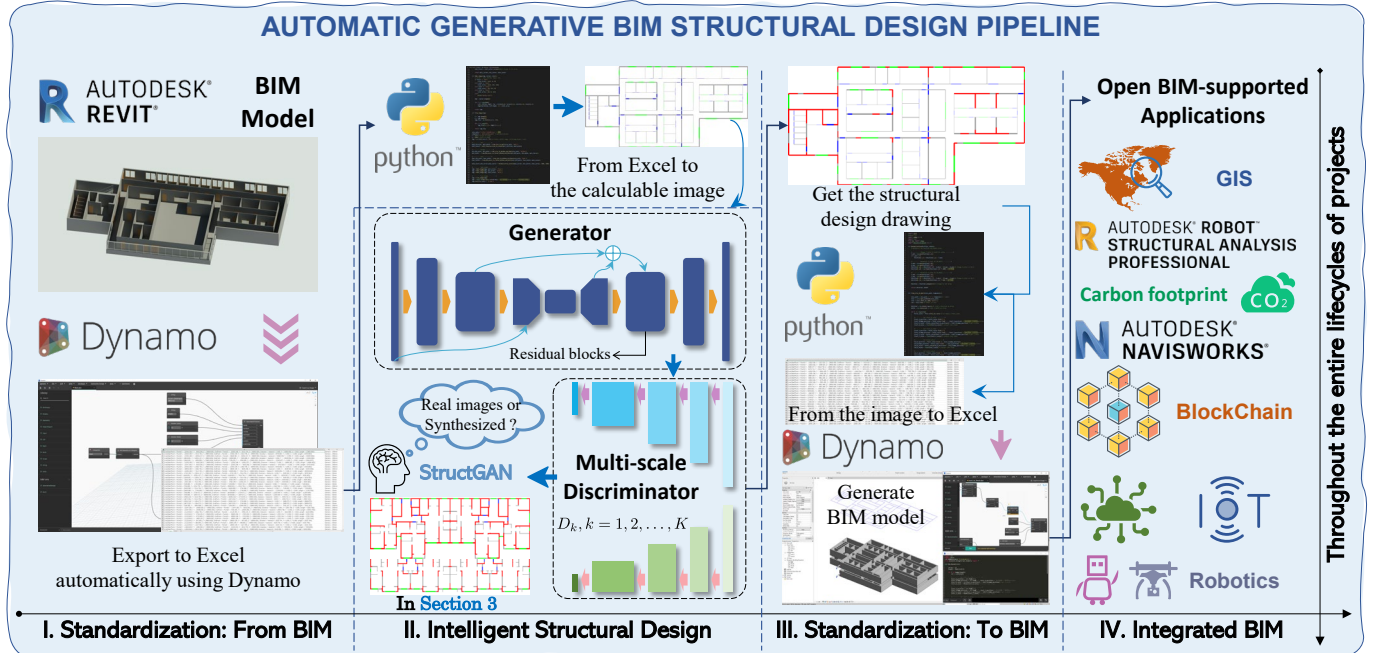


Fig. 2. The overall framework of the structural design pipeline integrating BIM and generative AI.

### 2.1. Motivation

It is known that the workflow of StructGAN [1] can be mainly summarized into three parts: (1) from CAD drawings to architectural design drawings (also named calculable images in the paper), (2) from architectural design drawings

to structural design drawings, and (3) from structural design drawings to models. Architectural design drawings and structural design drawings are the absolute core parts of StructGAN, and its open-sourced dataset just consists of these two parts. Because this research always wants to align with StructGAN and is dedicated to promoting the universality and scalability of structural smart design together with StructGAN and its variants, architectural design drawings and structural design drawings are kept in this research. Therefore, similar to StructGAN, the first three stages are: (1) from BIM to calculable images; (2) from calculable images to structural design drawings; and (3) from structural design drawings to BIM. The fourth stage is some representative applications integrating BIM, which cannot be achieved in StructGAN but easily benefit from the extraordinary scalability of BIM.

### *2.2. Standardization: From BIM*

First of all, we need a BIM model of the building given by BIM design software, such as Revit, one of the most widely used design, coordination, and management tools for BIM projects. The purpose of this stage is to create calculable images based on given BIM models in a standard way. Obviously, there hasn't been a direct way to achieve this goal. In order to solve this problem, let's think about it backwards. It's well known that Python is a very powerful computer language and can generate all kinds of images according to given data. Thus, Python can be adopted to generate calculable images based on architecture data. Subsequently, this question is transformed into how to get architecture data. Benefiting from the mature software ecosystem of Revit, we find that Dynamo, an open-source visual programming platform, can help us export design data to Excel files from BIM models, and then this problem is done. Firstly, Dynamo code is written to export data to Excel from BIM models automatically. Subsequently, a Python script is written to generate calculable images from Excel files. Although a little circuitous, this solution is effective. The future research plan is to develop a Revit plugin integrating these functions to facilitate engineers' operations.

### *2.3. Intelligent Structural Design*

Based on the calculable images obtained in the first stage, the objective of the second stage is to conduct smart structural design using generative AI, *i.e.*, generating structural design drawings with shear walls. Obviously, any generative AI methods can be embedded into this versatile framework, not only classical GAN-based methods (*e.g.*, StructGAN), but also the latest and most powerful diffusion model-based methods (researched in this paper). To pay tribute to the pioneer, StructGAN, its processing flow is selected as a representative method (see [Fig. 2](#)). StructGAN trains a generator and a multi-scale discriminator in an alternating and adversarial way, following pix2pixHD. The generator is used to generate synthetic images based on calculable images, and the function of the discriminator is to judge whether images are real labels or fake synthesized images. Although this classical processing flow can generate images looking like the labels, the images' visual quality is not satisfying, and complex post-processing and image fine-tuning are requisite. Inspired by the process of human drawing, this paper designs a 2-stage generation framework, and as one of the core contributions, the framework is going to be elaborated in the following [Section 3](#).

### *2.4. Standardization: To BIM*

Although structural design drawings are obtained by the second stage, BIM models are fundamentals of BIM projects and BIM-supported applications. Thus, the third stage wants to reproduce 3-dimensional (3D) BIM models from synthesized images, and the only difference is that the new BIM models contain structural information compared with the initial models in the first stage. Therefore, this stage can be roughly understood as the inverse process of the first stage: firstly, Excel files are obtained from structural design drawings by Python code; secondly, Dynamo code is adopted to generate BIM models from Excel files. It is worth noting that all the Python code and

Dynamo code in Section 2 can be available at <https://github.com/hzlbbfrog/Generative-BIM>.

### 2.5. BIM-integrated applications

Benefiting from its powerful scalability, BIM has been integrated with all kinds of advanced technologies to play a beneficial role throughout the entire lifecycle of projects, *i.e.*, planning, design, construction, and operation and maintenance [35]. Since BIM projects have been generated in the third stage, the advantages of BIM can be leveraged on this basis. The fourth stage revisits representative BIM-integrated applications throughout projects' life cycles.

For example, in the planning stage, we can integrate BIM and the geographic information system (GIS) to enable effective management and analysis of spatial data [35]. In the architecture and building design stage, besides adopting BIM design tools, such as Revit introduced before, to finish architecture designs efficiently, we can also utilize structural analysis software, *e.g.*, Robot Structural Analysis Professional, to check structural safety, including static analysis, dynamic analysis, etc. BIM technologies can also be used to calculate the carbon footprints of buildings [48] to explore sustainable and environmental-friendly low-carbon designs [49]. In the construction stage, BIM review and coordination software can be used to improve project delivery. For example, Navisworks can visualize and unify design and construction data and identify and resolve clash and interference problems. Besides, blockchain technology can also be integrated into BIM to better conduct construction process management, such as supply chain management and contract management [50]. In the operation and maintenance stage, the integration of Internet of Things (IoT) [51] sensors and BIM can provide real-time monitoring and supervision to facilitate project management [52]. Some researchers also combine robotics, such as unmanned ground vehicles (UGVs) [53] and unmanned aerial vehicles (UAVs) [54], with BIM to improve the efficiency of facility inspection [55].

## 3. Generation framework of structural design drawings

In the traditional end-to-end generation framework proposed in [1] (*i.e.*, the StructGAN paper), architectural design drawings are the inputs of AI models, and AI models are trained to synthesize structural design drawings close to the true structural design drawings in one step. This paper considers this generation problem from a new perspective and proposes a novel 2-stage generation framework (see Fig. 3). The motivation and interpretation are presented next in detail.

First of all, let's revisit the core research objectives in the traditional framework: architectural design drawings and structural design drawings. There are 3 components in architectural drawings, namely, nonstructural infill walls, windows, and outdoor gates, and they are represented by grey pixels (RGB tuple=(152,152,152)), green pixels (RGB tuple=(0,255,0)), and blue pixels (RGB tuple=(0,0,255)), respectively. The remaining area represented by white pixels (RGB tuple=(255,255,255)) is empty. Compared with architectural drawings, there is a new component in structural design drawings, *i.e.*, structural shear walls represented by red pixels (RGB tuple=(255,0,0)). It is obvious that the set of shear walls in structural design drawings is a subset of the set of infill walls in architectural drawings; namely, the essence of this generation problem is to infer shear walls (red pixels) from infill walls (grey pixels).

The traditional framework wants AI models to predict structural design drawings directly; that is to say, it wants models to finish the following 3 task simultaneously and successfully: (1) choose appropriate pixels from the grey pixels and change the color to red; (2) ensure that the models don't change the RGB tuples of unselected grey pixels; and (3) ensure that the models don't change the RGB tuples of green, blue, and white pixels. We can understand these generation tasks from another perspective: the traditional framework wants AI models to "draw" key objects (*i.e.*, red shear walls) on a semi-finished painting (*i.e.*, a semantic drawing) without changing any other parts. These tasks are arduous for GANs with limited representation power, so it is clear that the generation results

are not satisfactory (see Fig. 1). Since we have found the latent relationship between generation tasks and drawing, a question arises: can we borrow some inspiration from drawing to make generating tasks easier to solve? Following the idea, this paper makes some explorations.

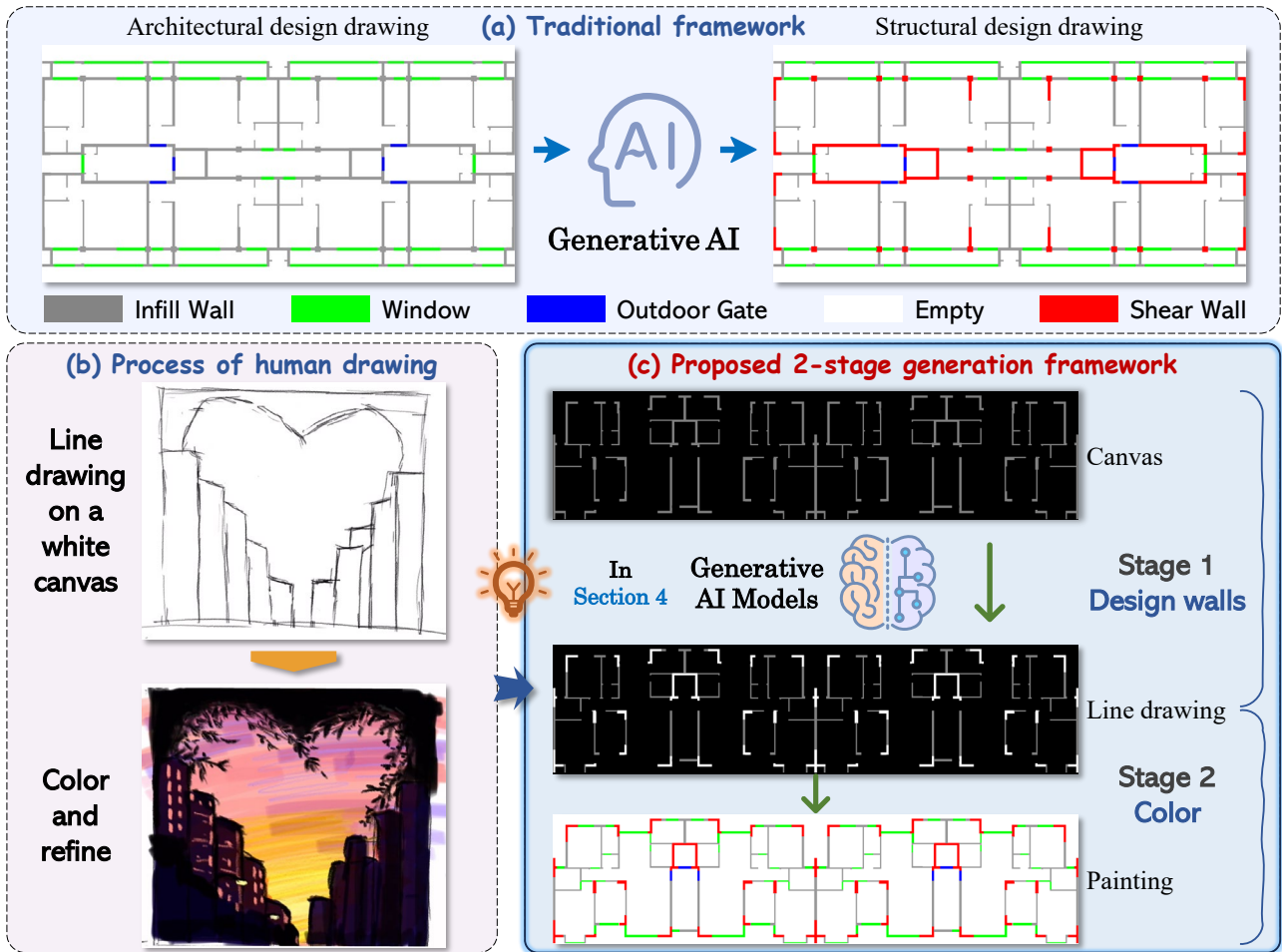


**Fig. 3.** The proposed 2-stage generation framework: (a) the traditional framework, (b) the process of human drawing, and (c) the new 2-stage generation framework.

As shown in Fig. 3 (b), let's first revisit the most common drawing process, which is also easiest to implement for humans: (1) prepare a white canvas; (2) draw essential lines on the canvas; and (3) color and refine. Inspired by this process, a 2-stage generation framework is designed (see Fig. 3 (c)). At first, a canvas is prepared. Compared with original architectural drawings, this canvas only retains infill walls, *i.e.*, grey pixels in Fig. 3 (c) and removes other components to simplify the task. This simplification is reasonable because, on the one hand, only infill walls are changed throughout the generation process, so we need to keep them; on the other hand, gates and windows don't affect structural designs (theoretically, we can even arbitrarily add or delete doors or windows in gaps in walls), so removing them is feasible. Besides, original three-channel RGB images are also compressed to single-channel images to reduce the dimensionality of image data. Then, in the first stage, the task of AI models is just to pick appropriate pixels as shear walls and change their color from grey to white, which is just like painting a line drawing. In the second stage, according to previous analysis, we have known that gates and windows aren't changed throughout the process, so we just need to color the line drawing and then paint gates and windows, referring to the initial architectural drawing, to obtain the final structural design drawing. Simple code can achieve this goal without training any models.



Obviously, AI models' task is to paint a line drawing based on a given canvas, and the complexity of the generation problem is greatly simplified. Besides, DMs with the most powerful generation and representation capability are introduced to replace GANs, and details of DMs are going to be expounded in the following [Section 4](#). Experiments in [Section 6](#) corroborate the effectiveness of the proposed generation framework.

#### 4. Conditional diffusion model considering physical conditions

**Notations.** Because there are many notations starting from this section, let's briefly introduce the notation rules adopted in this paper to reduce the confusion. The random vectors, random matrices, or tensors in the neural networks are denoted by non-tilt boldface upper case letters, such as  $\mathbf{X}$  and  $\mathbf{M}$ . Vectors or specific values of random vectors are all denoted by non-tilt boldface lower case letters, such as  $\mathbf{x}$  and  $\mathbf{y}$ . Scalars are represented by tilt non-bold lower-case letters, such as  $x$  and  $y$ . Besides, vectors are all column vectors, namely,  $\mathbf{x} = [x_1, \dots, x_N]^T$  is adopted to represent the vector  $\mathbf{x}$  formed by  $N$  scalars.

Additionally, let's introduce a key assumption before starting, which is widely accepted and adopted in machine learning research.

**Assumption 1 (Independence Assumption).** All the random variables in random matrices are mutually independent.

According to Assumption 1, the random matrix  $\mathbf{X}_t \in \mathbb{R}^{1 \times H \times W}$  can be equivalently transformed into a random vector\*  $\mathbf{X}_t \in \mathbb{R}^D$ , where  $D = 1 \times H \times W$ . Because random vectors are much simpler than random matrices, the research objects are all random vectors transformed from random matrices in this study, unless otherwise clarified.

##### 4.1. Motivation of PCDM

As clarified in [Section 1](#), DMs are currently one of the hottest deep learning methods and have more powerful image synthesis capability than GAN, which held the SOTA on image generation tasks before. Therefore, DMs are selected as the basic generative model in this research.

Further, conventional DMs try to learn and model the underlying data distribution  $q_0(\mathbf{x})$ , from image data  $\mathbf{x}$  by performing variational inference on a Markovian process; namely, they can be approximatively considered a Markovian hierarchical variational autoencoder [56]. Let the learned new distribution be  $p_\theta(\mathbf{x})$  with parameters  $\theta$ ; namely, it is a parametric approximation [15] to a real data distribution  $q_0(\mathbf{x})$ . Subsequently, DMs sample new samples from the modeled data distribution  $p_\theta(\mathbf{x})$  to achieve the goal of generation. In the paradigm of conventional DMs, the sampling is random and cannot be controlled. The generation problem researched in this paper needs to ensure that the positions of walls are not changed before and after generation (see Stage 1 in [Fig. 3](#) (c) for a more intuitive understanding). Obviously, this is intractable under the traditional DM framework. In order to solve this problem, conventional DMs are extended to conditional diffusion models (CDMs) [14][15][56], where the modeling objective is changed to a conditional distribution  $p_\theta(\mathbf{x}|\mathbf{y})$  so that we can explicitly control generation results through conditional information  $\mathbf{y}$ . In this paper,  $\mathbf{x} \in \mathbb{R}^D$  represents the line drawing,  $\mathbf{y} \in \mathbb{R}^D$  means the canvas, and  $D = 1 \times H \times W$ , where 1 indicates that the channel of images is 1, and  $H$  and  $W$  represent the height and width of images, respectively.

Ulteriorly, it is obvious that the ratios of shear walls are different for different heights and different seismic precautionary intensities. For example, we obviously need to design more shear walls for the buildings constructed in zones with 8-degree seismic precautionary intensity than those built in zones with 7-degree seismic precautionary

---

\* The notation  $\mathbf{X}_t$  is kept here for notation simplicity.

intensity. Here, 8-degree and 7-degree seismic precautionary intensities mean the design basic acceleration values of ground motion in the corresponding zones are  $0.20\sim 0.30g$  and  $0.10\sim 0.15g$ , respectively, following the Chinese General Code for Seismic Precaution of Buildings and Municipal Engineering [57] and the Chinese Code for Seismic Design of Buildings [58].  $g$  represents the gravitational acceleration. In order to guide the generation of the AI model and don't let it design shear walls arbitrarily, physical conditions, denoted as  $d$ , integrating heights and seismic design intensities, are embedded in the CDM, and then the modeling objective is further changed into  $p_{\theta}(\mathbf{x}|\mathbf{y}, d)$ . To simplify notations, this kind of DM is named PCDM (i.e., physics-based conditional diffusion model). Details of PCDM are delineated below.

#### 4.2. Preliminary of PCDM

Let's revisit DMs and CDMs before introducing PCDM to convey some necessary preliminary knowledge.

Firstly, conventional DMs progressively add Gaussian noise to the original clean image, denoted as  $\mathbf{x}$  or  $\mathbf{x}_0$ , by a fixed  $T$ -step Markov chain to obtain a list consisting of noisy samples  $[\mathbf{x}_1, \mathbf{x}_2, \dots, \mathbf{x}_T]$ . The transition probability between adjacent timesteps is denoted as  $q(\mathbf{x}_t|\mathbf{x}_{t-1})$ . This adding-noise process is usually named the forward diffusion process [59] or the Gaussian diffusion process [15]. DMs then model a transition distribution  $p_{\theta}(\mathbf{x}_{t-1}|\mathbf{x}_t)$  based on a learned denoising model  $g_{\theta}(\mathbf{x}_t)$ . Subsequently, according to  $p_{\theta}(\mathbf{x}_{t-1}|\mathbf{x}_t)$ , DMs recover clean samples from Gaussian noise iteratively via a reverse Markov chain. This denoising process is usually named the reverse denoising process [44] or the reverse diffusion process [59]. The process of modeling  $p_{\theta}(\mathbf{x}_{t-1}|\mathbf{x}_t)$  and  $g_{\theta}(\mathbf{x}_t)$  is named optimization process in this study because of its optimization nature.

CDMs maintain the forward diffusion process of DMs. However, in the optimization process, they model a new transition kernel conditioned on  $\mathbf{y}$ , denoted  $p_{\theta}(\mathbf{x}_{t-1}|\mathbf{x}_t, \mathbf{y})$  based on a new denoising model with condition information  $g_{\theta}(\mathbf{x}_t, \mathbf{y})$ . Then, in the reverse denoising process, the transition probability is also substituted with  $p_{\theta}(\mathbf{x}_{t-1}|\mathbf{x}_t, \mathbf{y})$ .

PCDM keeps the main settings in CDMs, but the core difference is that the physical information is further introduced into the conditional transition kernel; namely, the new conditional transition kernel is  $p_{\theta}(\mathbf{x}_{t-1}|\mathbf{x}_t, \mathbf{y}, d)$ . Therefore, PCDM also consists of three parts, i.e., the forward diffusion process, the reverse denoising process, and the optimization process, which are detailed in the following subsections.

#### 4.3. Forward diffusion process

In the forward process, we want to inject a small amount of Gaussian noise  $\epsilon \in \mathbb{R}^D$  step-by-step by a  $T$ -step Markov chain as shown in Fig. 4. Following [59], the transition probability is defined as

$$q(\mathbf{x}_t|\mathbf{x}_{t-1}) \triangleq \mathcal{N}(\mathbf{x}_t; \sqrt{1 - \beta_t}\mathbf{x}_{t-1}, \beta_t \mathbf{I}_D). \quad (1)$$

It is important to note that random variables in the Gaussian noise  $\epsilon$  are all independently sampled from the standard normal distribution, so the mean value is 0, and the covariance matrix is an identity matrix, namely,  $\epsilon \sim \mathcal{N}(0, \mathbf{I}_D)$ , where  $\mathbf{I}_D$  denotes the identity matrix in  $\mathbb{R}^{D \times D}$ .  $\beta_t$  is the noise schedule to control the amount of noise for different timestep, and  $\beta_t \in (0, 1)$  for  $\forall t \in \{1, \dots, T\}$ . In original DDPM,  $\beta_t$  is designed as a linear noise schedule. DDPM+ [60] finds that the linear schedule can cause the end of the forward process to be too noisy, which means that it cannot make a significant contribution to sample quality. Therefore, DDPM+ proposes a cosine schedule to alleviate this problem. This paper also substitutes the linear schedule with the cosine schedule. Firstly, define a function  $\bar{\alpha}_t$  over timesteps:

$$g(t) \triangleq \cos^2\left(\frac{t/T + s}{1 + s} \times \frac{\pi}{2}\right), \quad (2)$$

$$\bar{\alpha}_t \triangleq \frac{g(t)}{g(0)}, \quad (3)$$

where  $s$  is a small offset. Then,  $\beta_t$  can be calculated based on  $\bar{\alpha}_t$ :

$$\beta_t = 1 - \frac{\bar{\alpha}_t}{\bar{\alpha}_{t-1}}. \quad (4)$$

In the optimization process (refer to [Subsection 4.5](#) to get a clearer understanding), we need to uniformly sample timesteps repeatedly to train the denoising model, and for each sampling, we all need to get the corresponding noisy sample. For example, we sample a  $t_0 \in \{1, \dots, T\}$  and then we want to obtain  $\mathbf{x}_{t_0}$ . If just according to Eq. (1), we have to sample  $t_0$  times iteratively to get  $\mathbf{x}_{t_0}$ . It is so time-consuming and needs too many computing resources. Owing to the nice properties of the Gaussian distribution, we can get the closed-form expression of  $q(\mathbf{x}_t|\mathbf{x}_0)$  so that  $\mathbf{x}_t$  can be directly sampled for arbitrary  $t$ :

$$\mathbf{x}_t \sim q(\mathbf{x}_t|\mathbf{x}_0) = \mathcal{N}(\mathbf{x}_t; \sqrt{\bar{\alpha}_t}\mathbf{x}_0, (1 - \bar{\alpha}_t)\mathbf{I}_D). \quad (5)$$

The derivation process for the above equation is detailed in [Appendix A.1](#). As for how to sample, the reparameterization trick [20] can be applied to achieve this easily:

$$\mathbf{x}_t = \sqrt{\bar{\alpha}_t}\mathbf{x}_0 + \sqrt{1 - \bar{\alpha}_t}\boldsymbol{\epsilon}. \quad (6)$$

where  $\boldsymbol{\epsilon} \sim \mathcal{N}(0, \mathbf{I}_D)$ . As  $t$  increases,  $g(t)$  is close to 0, namely,  $\bar{\alpha}_t$  is close to 0. Therefore,  $\mathbf{x}_0$  gradually loses distinguishable features and approaches a standard normal distribution when  $t$  is large enough, *i.e.*, approximately,  $\mathbf{x}_T \sim \mathcal{N}(0, \mathbf{I}_D)$ .

#### 4.4. Reverse denoising process

Literally, the reverse denoising process is the reverse process of the forward diffusion process. Specifically, the goal of the reverse denoising process is to regenerate clean samples  $\hat{\mathbf{x}}_0$  from Gaussian noise  $\hat{\mathbf{x}}_T \sim \mathcal{N}(0, \mathbf{I}_D)$  and make  $\hat{\mathbf{x}}_0$  follow the real data distribution  $q_0$  as much as possible, where the notation with hats means the estimated data. Therefore, the reverse denoising process can be considered an inference process or a sampling process. A clear illustration of this process can be found in [Fig. 4](#).

A key question is the value of the unknown  $T$ . Obviously, when  $T$  is large enough, approximately,  $\mathbf{x}_T \sim \mathcal{N}(0, \mathbf{I}_D)$ , so the difference between  $\mathbf{x}_T$  and  $\hat{\mathbf{x}}_T$  can be negligible, which is a prerequisite that the distribution of the reconstructed sample  $p(\hat{\mathbf{x}}_0)$  is close to or equal to  $q_0$ . Following SR3 [15], a representative study of DMs,  $T$  is set to 2000.

After obtaining  $\hat{\mathbf{x}}_T$ , it is clear that if we can further know  $q(\mathbf{x}_{t-1}|\mathbf{x}_t)$ , we can easily achieve this reconstruction goal by a reverse Markov chain. Therefore, another key question is how to compute  $q(\mathbf{x}_{t-1}|\mathbf{x}_t)$ . Frustratingly, it is intractable to get  $q(\mathbf{x}_{t-1}|\mathbf{x}_t)$  [59]. However, DDPM finds that if this probability is conditioned on  $\mathbf{x}_0$ , then it turns out to be tractable:

$$q(\mathbf{x}_{t-1}|\mathbf{x}_t, \mathbf{x}_0) = \mathcal{N}(\mathbf{x}_{t-1}; \tilde{\boldsymbol{\mu}}_t(\mathbf{x}_t, \mathbf{x}_0), \tilde{\boldsymbol{\Sigma}}_t), \quad (7)$$

where

$$\tilde{\boldsymbol{\mu}}_t(\mathbf{x}_t, \mathbf{x}_0) = \frac{\sqrt{1 - \beta_t}(1 - \bar{\alpha}_{t-1})}{1 - \bar{\alpha}_t}\mathbf{x}_t + \frac{\sqrt{\bar{\alpha}_{t-1}}\beta_t}{1 - \bar{\alpha}_t}\mathbf{x}_0, \quad (8)$$

and

$$\tilde{\boldsymbol{\Sigma}}_t = \tilde{\beta}_t\mathbf{I}_D, \tilde{\beta}_t = \frac{1 - \bar{\alpha}_{t-1}}{1 - \bar{\alpha}_t}\beta_t. \quad (9)$$

The key insight behind  $q(\mathbf{x}_{t-1}|\mathbf{x}_t, \mathbf{x}_0)$  is that firstly,  $q(\mathbf{x}_t|\mathbf{x}_{t-1}) = q(\mathbf{x}_t|\mathbf{x}_{t-1}, \mathbf{x}_0)$  due to the Markov property (*i.e.*, the memoryless property), and secondly, based on Bayes' rule,  $q(\mathbf{x}_t|\mathbf{x}_{t-1}, \mathbf{x}_0)$  can be rewritten as

$$q(\mathbf{x}_t|\mathbf{x}_{t-1}, \mathbf{x}_0) = \frac{q(\mathbf{x}_t|\mathbf{x}_0)q(\mathbf{x}_{t-1}|\mathbf{x}_t, \mathbf{x}_0)}{q(\mathbf{x}_{t-1}|\mathbf{x}_0)}. \quad (10)$$

According to Eq. (5),  $q(\mathbf{x}_t|\mathbf{x}_0)$  and  $q(\mathbf{x}_{t-1}|\mathbf{x}_0)$  can both be parameterized, and Eq. (1) gives the definition of  $q(\mathbf{x}_t|\mathbf{x}_{t-1})$ , i.e., the definition of  $q(\mathbf{x}_t|\mathbf{x}_{t-1}, \mathbf{x}_0)$ , so that  $q(\mathbf{x}_{t-1}|\mathbf{x}_t, \mathbf{x}_0)$  can be parameterized after a series of mathematical deductions. The detailed derivation of Eqs. (7), (8), and (9) can refer to [Appendix A.2](#).

Although the closed-form solution of  $q(\mathbf{x}_{t-1}|\mathbf{x}_t, \mathbf{x}_0)$  is obtained, we cannot still sample new data starting from  $\hat{\mathbf{x}}_T$  based on it. This is because  $\mathbf{x}_0$  is unknown in the sampling stage. Then AI comes. A direct idea is that if we can model a transition distribution  $p_\theta(\mathbf{x}_{t-1}|\mathbf{x}_t, \mathbf{y}, d)$  using a neural network with parameters  $\theta$  to approximate  $q(\mathbf{x}_{t-1}|\mathbf{x}_t, \mathbf{x}_0)$  then we can achieve the goal mentioned before with this new reverse Markov chain. Since  $\mathbf{y}$  and  $d$  are pre-given, and  $\hat{\mathbf{x}}_T$  can be sampled from  $\mathcal{N}(0, \mathbf{I}_D)$ , and if we assume  $p_\theta(\mathbf{x}_{t-1}|\mathbf{x}_t, \mathbf{y}, d)$  has been obtained,  $\hat{\mathbf{x}}_{T-1}$  can be easily obtained by sampling from  $p_\theta(\hat{\mathbf{x}}_{T-1}|\hat{\mathbf{x}}_T, \mathbf{y}, d)$ . Repeat this step, and the clean sample  $\hat{\mathbf{x}}_0$  can be finally obtained. This is just the whole view of the reverse denoising process, and it is summarized in [Algorithm 1](#). Because sampling is random, if we run the reverse denoising process multiple times, the  $\hat{\mathbf{x}}_0$  obtained each time will be different even if  $p_\theta$ ,  $\mathbf{y}$ , and  $d$  are all fixed. This means that for a trained PCDM, we can get “infinite” design drawings for the same input, and it is impossible for StructGAN because the prediction is also fixed if the model is fixed. Some examples are presented in the experimental section to show the diversity of results generated by PCDM.

---

**Algorithm 1** Reverse denoising process
 

---

**Require:** canvas  $\mathbf{y}$ , physical condition  $d$ , and  $p_\theta(\hat{\mathbf{x}}_{t-1}|\hat{\mathbf{x}}_t, \mathbf{y}, d)$

- 1: Sample  $\hat{\mathbf{x}}_T \sim \mathcal{N}(0, \mathbf{I}_D)$
  - 2: **for**  $t = T, T - 1, \dots, 1$  **do**
  - 3:   Sample  $\hat{\mathbf{x}}_{t-1} \sim p_\theta(\hat{\mathbf{x}}_{t-1}|\hat{\mathbf{x}}_t, \mathbf{y}, d)$
  - 4: **end for**
  - 5: **return**  $\hat{\mathbf{x}}_0$
- 

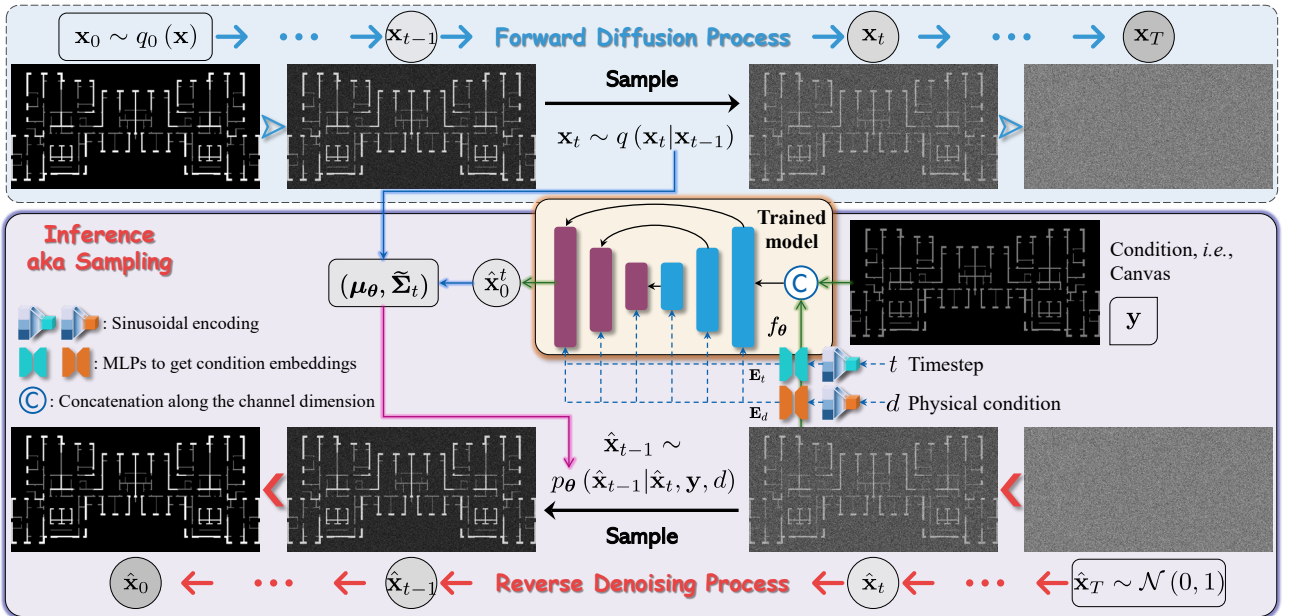


**Fig. 4.** Schematic diagram of forward diffusion process and reverse denoising process.

As regards how to train a neural network to get  $p_\theta(\mathbf{x}_{t-1}|\mathbf{x}_t, \mathbf{y}, d)$ , the next subsection is going to provide a detailed introduction.

#### 4.5. Optimization process: Parameterization of $p_\theta(\mathbf{x}_{t-1}|\mathbf{x}_t, \mathbf{y}, d)$ and training algorithm

We want to train a model with parameters  $\theta$  to make  $p_\theta(\mathbf{x}_{t-1}|\mathbf{x}_t, \mathbf{y}, d)$  close to  $q(\mathbf{x}_{t-1}|\mathbf{x}_t, \mathbf{x}_0)$  as much as possible. Since  $q(\mathbf{x}_{t-1}|\mathbf{x}_t, \mathbf{x}_0)$  is a Gaussian distribution, the simplest idea is to model  $p_\theta(\mathbf{x}_{t-1}|\mathbf{x}_t, \mathbf{y}, d)$  to be a Gaussian distribution as well:

$$p_\theta(\mathbf{x}_{t-1}|\mathbf{x}_t, \mathbf{y}, d) \triangleq \mathcal{N}(\mathbf{x}_{t-1}; \boldsymbol{\mu}_\theta(\mathbf{x}_t, t, \mathbf{y}, d), \boldsymbol{\Sigma}_\theta(\mathbf{x}_t, t, \mathbf{y}, d)), \quad (11)$$

where  $\boldsymbol{\mu}_\theta$  denotes the mean vector of  $p_\theta$ , and  $\boldsymbol{\Sigma}_\theta$  represents the covariance matrix of  $p_\theta$ . Because  $\mathbf{x}_t$  is a vector and doesn't include timestep information,  $t$  is explicitly embedded into  $\boldsymbol{\mu}_\theta$  and  $\boldsymbol{\Sigma}_\theta$  to introduce time information. Intuitively, we can minimize the distance between  $\boldsymbol{\mu}_\theta$  and  $\tilde{\boldsymbol{\mu}}_t$  and the distance between  $\boldsymbol{\Sigma}_\theta$  to  $\tilde{\boldsymbol{\Sigma}}_t$  to make  $p_\theta$  close to  $q$ . DDPM and DDPM+ find that if let  $\boldsymbol{\Sigma}_\theta$  be  $\tilde{\boldsymbol{\Sigma}}_t$ , namely,  $\boldsymbol{\Sigma}_\theta$  is not learnable, the sample quality will be almost unaffected, but the question is simplified. Following DDPM,  $\boldsymbol{\Sigma}_\theta$  is set to  $\tilde{\boldsymbol{\Sigma}}_t$  here, then we just need to minimize the distance between  $\boldsymbol{\mu}_\theta$  and  $\tilde{\boldsymbol{\mu}}_t$ . The classical MSE loss is adopted to measure the similarity:

$$\mathcal{L} = \mathbb{E}_{t \sim \text{Uniform}[1, T], \mathbf{x}_0, \epsilon \sim \mathcal{N}(0, \mathbf{I}_D)} \|\tilde{\boldsymbol{\mu}}_t - \boldsymbol{\mu}_\theta(\mathbf{x}_t, t, \mathbf{y}, d)\|_2^2, \quad (12)$$

where  $\text{Uniform}[1, T]$  means the uniform distribution. Because  $\tilde{\boldsymbol{\mu}}_t$  and  $\boldsymbol{\mu}_\theta$  are defined over  $t$ ,  $\mathbf{x}_0$ , and  $\epsilon$  (see Eqs. (6) and (8)),  $\mathcal{L}$  is an expectation value over  $t$ ,  $\mathbf{x}_0$ , and  $\epsilon$  to eliminate randomness.

Further, since  $\mathbf{x}_t$  has been known (it is a condition of  $p_\theta$ ) and  $\mathbf{x}_t$  is also included in  $\tilde{\boldsymbol{\mu}}_t$  (see Eq. (6)), we can consider keeping  $\mathbf{x}_t$  rather than predict the whole  $\boldsymbol{\mu}_\theta$  to reduce prediction difficulty. With this idea, we have two choices. The first choice is that we can build a neural network  $f_\theta$  to predict  $\mathbf{x}_0$ , and the prediction is denoted as  $\hat{\mathbf{x}}_0^t$ . Then, the new loss function is

$$\mathcal{L}_{\mathbf{x}_0} = \mathbb{E}_{t, \mathbf{x}_0, \epsilon} \|\mathbf{x}_0 - f_\theta(\mathbf{x}_t, t, \mathbf{y}, d)\|_2^2. \quad (13)$$

Next,  $\boldsymbol{\mu}_\theta$  can be directly derived based on  $f_\theta$  (refer to Eq. (8)):

$$\boldsymbol{\mu}_\theta = \frac{\sqrt{1 - \beta_t}(1 - \bar{\alpha}_{t-1})}{1 - \bar{\alpha}_t} \mathbf{x}_t + \frac{\sqrt{\bar{\alpha}_{t-1}}\beta_t}{1 - \bar{\alpha}_t} f_\theta(\mathbf{x}_t, t, \mathbf{y}, d). \quad (14)$$

Then, plug Eq. (14) into Eq. (11) to get the whole transition distribution:

$$p_\theta(\mathbf{x}_{t-1}|\mathbf{x}_t, \mathbf{y}, d) = \mathcal{N}\left(\mathbf{x}_{t-1}; \frac{\sqrt{1 - \beta_t}(1 - \bar{\alpha}_{t-1})}{1 - \bar{\alpha}_t} \mathbf{x}_t + \frac{\sqrt{\bar{\alpha}_{t-1}}\beta_t}{1 - \bar{\alpha}_t} f_\theta(\mathbf{x}_t, t, \mathbf{y}, d), \tilde{\beta}_t \mathbf{I}_D\right). \quad (15)$$

According to this transition, we can run the reverse denoising process (see [Subsection 4.4](#)) to generate new samples.

The second choice is that we firstly plug Eq. (6) into Eq. (8) to eliminate  $\mathbf{x}_0$ :

$$\tilde{\boldsymbol{\mu}}_t(\mathbf{x}_t, \mathbf{x}_0) = \frac{1}{\sqrt{1 - \beta_t}} \left( \mathbf{x}_t - \frac{\beta_t}{\sqrt{1 - \bar{\alpha}_t}} \epsilon \right). \quad (16)$$

The derivation of the above formula is detailed in [Appendix A.3](#). We then can build a neural network  $\epsilon_\theta$  to predict  $\epsilon$ , and the corresponding loss function is

$$\mathcal{L}_\epsilon = \mathbb{E}_{t, \mathbf{x}_0, \epsilon} \|\epsilon - \epsilon_\theta(\mathbf{x}_t, t, \mathbf{y}, d)\|_2^2. \quad (17)$$

Imitating the first choice,  $\boldsymbol{\mu}_\theta$  and  $p_\theta$  can also be represented by  $\epsilon_\theta$ :

$$\boldsymbol{\mu}_\theta = \frac{1}{\sqrt{1 - \beta_t}} \left( \mathbf{x}_t - \frac{\beta_t}{\sqrt{1 - \bar{\alpha}_t}} \epsilon_\theta(\mathbf{x}_t, t, \mathbf{y}, d) \right). \quad (18)$$

$$p_\theta(\mathbf{x}_{t-1}|\mathbf{x}_t, \mathbf{y}, d) = \mathcal{N}\left(\mathbf{x}_{t-1}; \frac{1}{\sqrt{1 - \beta_t}} \left( \mathbf{x}_t - \frac{\beta_t}{\sqrt{1 - \bar{\alpha}_t}} \epsilon_\theta(\mathbf{x}_t, t, \mathbf{y}, d) \right), \tilde{\beta}_t \mathbf{I}_D\right). \quad (19)$$

Obviously, these two methods are theoretically equivalent because optimization objectives are both to make  $\boldsymbol{\mu}_\theta$  close to  $\tilde{\boldsymbol{\mu}}_t$ , namely,  $p_\theta(\mathbf{x}_{t-1}|\mathbf{x}_t, \mathbf{y}, d)$  close to  $q(\mathbf{x}_{t-1}|\mathbf{x}_t, \mathbf{x}_0)$ . However, it is worth noting that in practice, the second choice is applied in the most DMs-based methods, such as DDPM, DDPM+, DDIM [25], Stable Diffusion [44], etc., because the choice pays more attention to **variability** by estimating noise. However, this paper hopes that DMs can focus on **similarity** to generate realistic structural design drawings. Therefore, this paper takes

the first choice, *i.e.*, estimating  $\mathbf{x}_0$ . The above algorithm is summarized in [Algorithm 2](#) for better explanation. The upper parts of [Fig. 5](#) also introduce the training process in the form of graphics, which is also worth referring to for gaining a vivid understanding of the entire optimization process.

---

**Algorithm 2** Training of PCDM
 

---

**Require:** denoiser network  $f_\theta$ , noise schedule  $\{\bar{\alpha}_t\}_{t=1}^T$  and  $\{\beta_t\}_{t=1}^T$

- 1: Initialize model parameters  $\theta$
- 2: **while** not converged **do**
- 3:     **Input** line drawing  $\mathbf{x}_0$ , canvas  $\mathbf{y}$ , physical condition  $d$
- 4:      $t \sim \text{Uniform}\{1, \dots, T\}$
- 5:      $\epsilon \sim \mathcal{N}(0, \mathbf{I}_D)$
- 6:      $\mathbf{x}_t \leftarrow \sqrt{\bar{\alpha}_t} \mathbf{x}_0 + \sqrt{1 - \bar{\alpha}_t} \epsilon$    ▷ Run forward diffusion process to get noisy sample
- 7:      $\hat{\mathbf{x}}_0^t \leftarrow f_\theta(\mathbf{x}_t, t, \mathbf{y}, d)$
- 8:     Perform gradient descent step on  
            $\nabla_{\theta} \|\mathbf{x}_0 - \hat{\mathbf{x}}_0^t\|^2$
- 9: **end while**
- 10: **return**  $f_\theta$

---

Besides, in this subsection, we just claim the correctness of the parameterization of  $p_\theta(\mathbf{x}_{t-1} | \mathbf{x}_t, \mathbf{y}, d)$  from an intuitive perspective. Strict proofs are given in [Appendix B](#). If readers find it is a little tricky, you can skip [Appendix B](#), which doesn't affect your understanding of this research or DMs.

#### 4.6. Optimization process: Design of the neural network

The subsection focuses on how to build a denoising network  $f_\theta$  to output  $\hat{\mathbf{x}}_0^t$  given a tuple  $(\mathbf{x}_t, t, \mathbf{y}, d)$ . Specifically, 3 tasks are researched and finished in this subsection. Firstly, [Subsection 4.1](#) has analyzed the importance of introducing the physical condition  $d$ , and this subsection studies how to effectively model  $d$ . Secondly, conditions  $t$ ,  $d$  and  $\mathbf{y}$  are totally different in terms of data dimensions and information provided, which shows they cannot be embedded into  $f_\theta$  in a consistent and easy way. This subsection studies how to effectively plug the conditions into  $f_\theta$ . Thirdly, this subsection also provides a detailed design for fusing cross-domain data.

##### 4.6.1. Physical condition and its superiority

**Physical condition in PCDM.** As introduced in [Subsection 4.1](#), the ratios of shear walls are obviously different for different seismic precautionary intensities and different heights. StructGAN's datasets consider 7-degree (*i.e.*, Group7 Dataset) and 8-degree (*i.e.*, Group8 Dataset) seismic precautionary intensities since 7-degree and 8-degree are the design criteria for most zones in China. Besides, structural heights are also a dominant factor for designing shear walls in 7-degree seismic precautionary zones [1]. Therefore, in StructGAN, the Group7 Dataset is further divided into two sub-datasets: Group7-H1 for the buildings whose heights are less than or equal to 50 *m* and Group7-H2 for those buildings whose heights > 50 *m* following structural height regulations in the Chinese Technical Specification for Concrete Structures of Tall Buildings [61]. In general, there are 3 sub-datasets provided in StructGAN: Group7-H1 (7-degree and heights  $\leq 50$  *m*), Group7-H2 (7-degree and heights > 50 *m*), and Group8 (8-degree). PCDM is trained on the same dataset and assigns different physical conditions to different sub-datasets to consider differences. Specifically, we have known that 7-degree and 8-degree mean the design basic acceleration values are 0.10~0.15*g* and 0.20~0.30*g*, respectively. Let  $g = 10$  *m/s*<sup>2</sup> roughly, then the design basic acceleration values are 1.0~1.5 *m/s*<sup>2</sup> and 2.0~3.0 *m/s*<sup>2</sup>, respectively. Therefore, we simply assign 1.0 to

Group7-H1, 1.5 to Group7-H2, and 2.5 to Group8 as physical conditions. Obviously, if physical conditions are finely tuned based on the characteristics of the datasets or are expanded to higher dimensions to consider the influences of heights, precautionary intensities, or other factors, such as construction sites and the importance of architectures (referring to the Chinese General Code [57]), simultaneously and finely, models' performance can be improved further. Here, we leave this investigation to future work.

**Superiority.** To avoid the impact of data variability among sub-datasets, StructGAN trains 3 models based on 3 sub-datasets, respectively. However, this also brings 2 outstanding drawbacks: (1) The amount of data is insufficient for each separate model, which may cause overfitting and hinder the performance of models. (2) It neglects the beneficial effects of data similarity among sub-datasets. Therefore, StructGAN-AE [3] introduces a pre-trained strategy, and the whole training includes 2 stages. Stage 1: pre-training stage. Models are trained based on the mixed data consisting of 3 sub-datasets in this stage. Stage 2: individual training stage. The pre-trained models are re-trained on 3 sub-datasets. Obviously, this solution is still not very elegant. Firstly, it needs at least 4 training sessions (once for pre-training and 3 times for individual training) to make models “see” all the data. Then, it needs to save 3 models (1 model per sub-dataset). A question: *is there a method where a single model can just “see” and analyze all the data by 1 training?* PCDM can achieve this. Because PCDM assigns different physical conditions to images coming from different sub-datasets, it can be trained on the entire dataset (*i.e.*, a mixed dataset including all the 3 sub-datasets) in the training stage. In the inference stage, PCDM can generate structural designs meeting inputted physical conditions, which also means that for the same input image, predicted results will change accordingly if inputted physical conditions change. For example, if a test image originally belongs to Group7-H1, PCDM can generate the right structural designs when the inputted condition is 1.0. Further, for the same test image, if the physical condition is changed from 1.0 to 2.5, PCDM with powerful generative ability can still generate a structural design drawing satisfying the new condition, which can bring great flexibility in design. Obviously, StructGAN and StructGAN-AE cannot have such generative capacity and achieve these functions which are limited by the nature of GAN methods. Some examples are presented in the experimental section.

#### 4.6.2. Condition embedding

The conditions of DMs can usually be divided into 2 categories. The first type of condition is global conditions, such as text descriptions and time information, to provide global information. The second type of condition is named local conditions, such as sketches, depth maps, and masks, to provide refined guidance considering local details. Some studies [62][63] recommend that global conditions are suitable to be projected into vector embeddings and then plug the latent embeddings into convolution blocks or attention blocks to provide high-density control. Local conditions are suitable to be concatenated with noisy samples and then sent into neural networks, which can ensure spatial sizes remain unchanged to keep complete and detailed information.

As analyzed before, there are 3 conditions needed to be considered in PCDM, namely, the timestep  $t$ , canvas  $\mathbf{y}$ , and physical condition  $d$ , among which  $t$  and  $d$  belongs to global conditions, and  $\mathbf{y}$  is a local condition. Therefore, as shown in Fig. 5, for  $t$  and  $d$ , we first map them into latent embeddings and then plug embeddings into residual blocks (*i.e.*, Res-Block or RB in Fig. 5) and attention blocks (*i.e.*, AB in Fig. 5). Residual blocks and attention blocks are expounded in the next subsection. The mapping of global conditions includes 2 steps as shown in the middle parts of Fig. 4 and the top parts of Fig. 5. The first step is the sinusoidal encoding, whose idea borrows from Transformer [64]. Taking  $t$  as an example, the sinusoidal encoding encodes this number into a  $D_t^{\text{En}}$ -dimensional vector  $\mathbf{En}_t \in \mathbb{R}^{D_t^{\text{En}}}$ :

$$\mathbf{En}_t[i] = \begin{cases} \cos\left(t \times P \frac{i-1}{\frac{D_t^{\text{En}}}{2}}\right) & 1 \leq i \leq \frac{D_t^{\text{En}}}{2} \\ \sin\left(t \times P \frac{(i-\frac{D_t^{\text{En}}}{2})-1}{\frac{D_t^{\text{En}}}{2}}\right) & \frac{D_t^{\text{En}}}{2} + 1 \leq i \leq D_t^{\text{En}} \end{cases}, \quad (20)$$

where  $D_t^{\text{En}}$  is even, and we set  $D_t^{\text{En}} = 32$  in all the experiments,  $P$  is a period constant and is set to 10000.  $\mathbf{En}_d \in \mathbb{R}^{D_d^{\text{En}}}$  where  $D_d^{\text{En}}$  is also set to 32 can be obtained by the same calculations. The second step is to map the 2 vectors to high-dimensional space by 2 MLPs. Specifically,  $\mathbf{En}_t$  is mapped into  $\mathbf{E}_t \in \mathbb{R}^{D_t}$ , and  $\mathbf{En}_d$  is projected into  $\mathbf{E}_d \in \mathbb{R}^{D_d}$ , where  $D_t = 3D_t^{\text{En}}$  and  $D_d = D_d^{\text{En}}$ . Here,  $\mathbf{E}_t$  and  $\mathbf{E}_d$  are just the condition embeddings to be plugged into the denoising network. Because the variation of  $t$  is greater than that of  $d$ , the dimension of  $\mathbf{E}_t$ ,  $D_t$ , is larger than that of  $\mathbf{E}_d$  to better represent the variation. For the local condition  $\mathbf{y}$ , plugging operations are simpler. It is first concatenated with the noisy sample  $\mathbf{x}_t$  to obtain the latent embedding  $(\mathbf{x}_t \cup \mathbf{y})$ , where  $\cup$  denotes a concatenation operation, and then the embedding is sent to the denoising network directly.

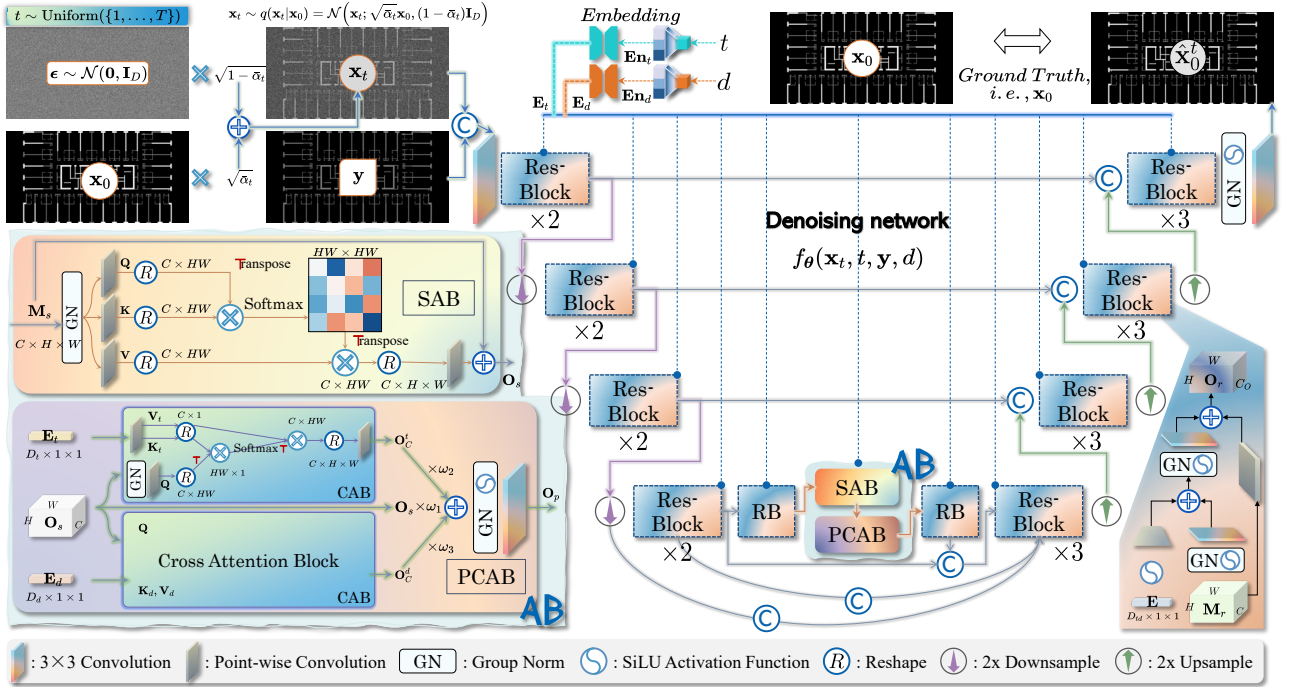


Fig. 5. Illustration of optimization process.

#### 4.6.3. Denoising network

U-shape networks represented by U-Net [65] have made significant success in DMs [14][15][25][42][44][60] due to their simplicity and effectiveness in feature fusion [66] and have almost become a de-facto standard backbone framework for DMs [67]. In light of these successful applications, the denoising network  $f_\theta(\mathbf{x}_t, t, \mathbf{y}, d)$  is also designed as a U-structure, as shown in Fig. 5. The core components are Res-Block (or RB) and AB of the network, and details of the two modules are delineated below.

**Res-Block or RB.** The function of Res-Blocks is to extract and fuse features from  $(\mathbf{x}_t \cup \mathbf{y})$  and  $(t, d)$ . Following the convention of DMs [60], an input of a Res-Block consists of 2 parts: the first part comes from previous blocks and is denoted as  $\mathbf{M}_r \in \mathbb{R}^{C \times H \times W}$ ; and the second part is the embedding of global conditions to strengthen the guidance effect of global conditions and is denoted as  $\mathbf{E}$ . Specifically,  $\mathbf{E}$  is the concatenation of  $\mathbf{E}_t$  and  $\mathbf{E}_d$



in this paper:

$$\mathbf{E} = \mathbf{E}_t \cup \mathbf{E}_d, \mathbf{E} \in \mathbb{R}^{D_{td}}, \quad (21)$$

where  $D_{td} = D_t + D_d$ . Next,  $\mathbf{E}$  is expanded to the matrix  $\mathbf{E} \in \mathbb{R}^{D_{td} \times 1 \times 1}$  to align with  $\mathbf{M}_r$  on dimensions to facilitate subsequent calculations. Then,  $\mathbf{E}$  goes through a SiLU [68] activation function to introduce nonlinearity and a point-wise convolution to change the channel, and an intermediate tensor  $\mathbf{E}' \in \mathbb{R}^{C_o \times 1 \times 1}$  is obtained, where  $C_o$  means the output channel. Similarly, after a Group Norm (GN) layer, a SiLU function, and a  $3 \times 3$  convolution, an intermediate tensor of  $\mathbf{M}_r$  is obtained, denoted as  $\mathbf{M}'_r \in \mathbb{R}^{C_o \times H \times W}$ .  $\mathbf{M}'_r$  and  $\mathbf{E}'$  are fused together by an element-wise addition operation where  $\mathbf{E}'$  is duplicated along the height and width directions of  $\mathbf{M}'_r$ . Following ResNet [69], a skip connection is introduced to merge intermediate data and the input feature map  $\mathbf{M}_r$  to solve the degradation problem [69] in deep networks. Finally, the output feature map of a Res-Block is obtained, denoted as  $\mathbf{O}_r \in \mathbb{R}^{C_o \times H \times W}$ .

**AB.** The inherent locality of convolutional operations enables convolutional neural networks (CNNs) to be good at modeling local information but concurrently poor at capturing global dependencies [70]. The self-attention mechanism can bring intrinsically global perception without the complex hierarchical stacking structures like those in CNNs and has been successfully applied to computer vision [71][72][73]. Further, researchers find that CNN+self-attention hybrid models can merit both the local perception of CNN and the capability of modeling long-range context features of self-attention, and many influential models have been proposed based on this, such as TransUNet [74] for medical image segmentation and BGCrack [70] for crack identification. Inspired by these applications, an AB is designed based on self-attention and embedded into the initial denoising network composed of CNN. As for the embedded position, as presented in Fig. 5, an AB is plugged into the high-level features, which is based on two considerations. On the one hand, high-level features have larger receptive fields, which bring more redundant long-term context information [70][75], so it is more effective to embed an AB into high-level features. On the other hand, since high-level features have a smaller spatial resolution, such an arrangement can also help reduce computation overhead [70]. The structure of the AB is presented next.

Specifically, the AB consists of 2 sub-modules: a self-attention block (SAB) and a parallel cross-attention block (PCAB) appended to the SAB. Firstly, the SAB conducts self-attention on the output of the previous RB, denoted as  $\mathbf{M}_s \in \mathbb{R}^{C \times H \times W}$ , to model the internal long-range relationship of the feature map:

$$\mathbf{O}_s = \text{SAB}(\mathbf{M}_s), \quad (22)$$

where  $\mathbf{O}_s$  represents the output feature map of the SAB. Subsequently, the PCAB takes  $\mathbf{O}_s$  and condition embeddings,  $\mathbf{E}_t$  and  $\mathbf{E}_d$ , as the inputs. It calculated the cross self-attention between  $\mathbf{O}_s$  and  $\mathbf{E}_t$ , and between  $\mathbf{O}_s$  and  $\mathbf{E}_d$  using 2 cross-attention blocks (CABs), respectively, to learn the latent global dependencies between the feature map and conditions:

$$\mathbf{O}_C^t = \text{CAB}(\mathbf{O}_s, \mathbf{E}_t), \quad (23a)$$

$$\mathbf{O}_C^d = \text{CAB}(\mathbf{O}_s, \mathbf{E}_d), \quad (23b)$$

where  $\mathbf{O}_C^t$  and  $\mathbf{O}_C^d$  are the outputs. Further, a parallel fusion strategy, borrowing from the successful experience in PAM [5] and BGCrack, is conducted to fuse multiple features:

$$\mathbf{M}_{Fuse} = w_1 \times \mathbf{O}_s + w_2 \times \mathbf{O}_C^t + w_3 \times \mathbf{O}_C^d, \quad (17)$$

where  $\mathbf{M}_{Fuse}$  is the fused feature map, and  $w_1$ ,  $w_2$ , and  $w_3$  are learnable parameters to adjust the weights. Then, a simple convolution block with the structure of “GN→SiLU→ $3 \times 3$  Conv” is applied to  $\mathbf{M}_{Fuse}$  to obtain the output of the PCAB  $\mathbf{O}_p \in \mathbb{R}^{C \times H \times W}$ . The calculation process for the AB is expounded in Appendix C.

## 5. Details of implementation

### 5.1. Dataset

The dataset used in this paper is named Modified-dataset. It is established based on the original open-sourced dataset [76] in StructGAN, which is named Original-dataset for convenience. The establishment process and details of Modified-dataset are described below. First, get images. The basic images in Modified-dataset all come from Original-dataset, namely, 63 images in the Group7-H1 sub-dataset, 55 images in the Group7-H2 sub-dataset, and 57 images in the Group8 sub-dataset. Second, resolution adjustment. Following StructGAN, the pixel resolution of images in Modified-dataset is adjusted to  $512 \times 1024$ . Third, color correction. We keenly notice that the colors of some areas in the partial image in Original-dataset don't match the expressions in the text (see Section 3 or StructGAN). Therefore, in this step, the RGB values of all the pixels in all the images are standardized to align with the RGB tuples in the paper. Fourth, data augmentation. Modified-dataset follows the same data augmentation strategy as that of Original-dataset, *i.e.*, each basic image is flipped vertically and horizontally and is rotated  $180^\circ$ . Therefore, after the augmentation, there are 252 images, 220 images, and 228 images in Group7-H1, Group7-H2, and Group8, respectively. Fifth, image combination. As mentioned in Subsection 4.6.1, PCDM can be trained on a mixed dataset, including all the 3 sub-datasets. To simplify the training process, Modified-dataset is adjusted further. Specifically, we add 3 identifiers to the names of images in 3 sub-datasets, such as "7degree" for the images in Group7-H1 and "8degree" for the images in Group8 to make it easy for PCDM to distinguish images from different sub-datasets. Then, we merge the 3 sub-datasets to build a new mixed dataset, which is just the final Modified-dataset, and now there are 700 images in the dataset. Modified-dataset is also open-sourced and available at <https://github.com/hzlbbfrog/Generative-BIM>.

## 5.2. Training and inference environment

The hardware used for training and testing is: an AMD Ryzen 7 5800X3D CPU, a Nvidia GeForce RTX 4090 GPU (24 GB), and 128 GB of RAM. The main software environment is: Windows 10 operating system, CUDA 11.6.2, CUDNN 8.6.0, and Python 3.8.15. The deep learning framework employs version 1.12.1 of PyTorch, developed by Meta.

## 5.3. Training policy

The Adam optimizer is utilized for training networks, and the hyper-parameters are set to the default values  $\beta = (0.9, 0.999)$ ,  $\varepsilon = 10^{-8}$  and  $weight\ decay = 0$ . The batch size is set to 1, and the learning rate is fixed at  $1 \times 10^{-4}$ . The networks are all trained for 70 epochs before inference. For simplicity, no additional data augmentation or learning rate schedulers are adopted in the training stage. It is worth noting that all the models are implemented in this unified training pipeline for fair comparisons, unless specified otherwise.

## 5.4. Evaluation metrics

To validate and evaluate the performance of the proposed models, two types of metrics are adopted, namely, an objective evaluation metric and a subjective evaluation metric. In StructGAN and its subsequent work, they only take the objective metric, namely,  $Score_{IoU}$ , which is calculated by comparing predictions with labels pixel by pixel but neglect subjective metrics. In fact, subjective metrics such as Inception Score (IS) [77] and Fréchet Inception Distance (FID) [78][79] are even more important because they can quantitatively evaluate the visual quality of generated samples by simulating human perception, namely, their values are consistent well with human judgment [80] and show whether the generation samples "look" real or not. Therefore, subjective metrics are introduced to judge if the generated drawings *look like* the structural design drawings designed by humans. Combining both metrics can result in a more accurate and thorough evaluation of the models' performance.

### 5.4.1. Objective metric

Following StructGAN and StructGAN-AE,  $Score_{IoU}$  is adopted to evaluate the generation results, which can be defined by the following formula:

$$Score_{IoU} = \eta_{SWratio} \times (\eta_{SIoU} \cdot SIoU + \eta_{WIoU} \cdot WIoU), \quad (25)$$

where  $\eta_{SIoU}$  and  $\eta_{WIoU}$  represent the weight coefficients of SIoU and WIoU and they are both set to 0.5. SIoU means the intersection over union (IoU) of shear walls, WIoU represents the weighted IoU, and  $\eta_{SWratio}$  denotes the correction coefficient for the overall quantity of shear walls, respectively. The three variables are defined as follows:

$$SIoU = \frac{A_{SWinter}}{A_{SWunion}}, \quad (26)$$

where  $A_{SWinter}$  is the intersection area of shear walls between predictions and labels, and  $A_{SWunion}$  is the corresponding union area.

$$WIoU = \sum_{i=0}^4 \frac{w_i p_{ii}}{\sum_{j=0}^4 p_{ij} + \sum_{j=0}^4 p_{ji} - p_{ii}}, \quad (27)$$

where  $i \in \{0, 1, \dots, 4\}$  means the category number and  $w_i$  represents the weight parameter of the class. Specifically,  $i = 0$  denotes black background, and  $w_0 = 0$ ,  $i = 1$  denotes shear walls and  $w_1 = 0.4$ ,  $i = 2$  denotes infill walls and  $w_2 = 0.4$ ,  $i = 3$  denotes windows, and  $w_3 = 0.1$ , and  $i = 4$  denotes outdoor gates and  $w_4 = 0.1$ .  $p_{ij}$  represents the number of pixels that actually belong to category  $i$  but are predicted to category  $j$ .

$$\eta_{SWratio} = \left( 1 - \frac{|SWratio_{pre} - SWratio_{label}|}{SWratio_{pre}} \right) \times 100\%, \quad (28)$$

where  $SWratio_{pre}$  and  $SWratio_{label}$  represents the ratios of shear walls in predictions and labels, respectively, and they can be calculated by the following formula:

$$SWratio = \frac{A_{SW}}{A_W}, \quad (29)$$

where  $SWratio$  includes  $SWratio_{pre}$  and  $SWratio_{label}$ ,  $A_{SW}$  represents the area of shear walls, and  $A_W$  denotes the area of walls, *i.e.*, shear walls + infill walls.

Based on the above definitions, we can see that  $Score_{IoU}$  is an objective metric and assess generation results by pixel-level comparison. It is clear that the larger the values of  $\eta_{SWratio}$ , SIoU, and WIoU, namely, the larger the value of  $Score_{IoU}$ , the closer the prediction is to the label.

#### 5.4.2. Subjective metric

IS and FID are the two most commonly used metrics to evaluate the perceptual quality of generated images. Considering FID is more robust to noise than IS [80], FID is adopted here.

Specifically, FID first embeds two image sets (*i.e.*, real images  $\mathbf{r}$  and generated images  $\mathbf{g}$ ) into high-level feature space given by a pre-trained Inception-V3 [81]. Then, FID views the feature space as a continuous multivariate Gaussian distribution and estimates the mean vector and covariance matrix of representations in the feature space of the real data and the generated data, respectively, denoted as  $(\boldsymbol{\mu}_r, \boldsymbol{\Sigma}_r)$  and  $(\boldsymbol{\mu}_g, \boldsymbol{\Sigma}_g)$ . Finally, the value of FID is the Fréchet distance between the two Gaussian distributions, namely,  $\mathcal{N}(\boldsymbol{\mu}_r, \boldsymbol{\Sigma}_r)$  and  $\mathcal{N}(\boldsymbol{\mu}_g, \boldsymbol{\Sigma}_g)$ , which gives the quantitative result of generation quality:

$$FID(\mathbf{r}, \mathbf{g}) = \|\boldsymbol{\mu}_r - \boldsymbol{\mu}_g\|_2^2 + \text{Tr} \left( \boldsymbol{\Sigma}_r + \boldsymbol{\Sigma}_g - 2\sqrt{\boldsymbol{\Sigma}_r \boldsymbol{\Sigma}_g} \right), \quad (29)$$

where  $\text{Tr}$  denotes the trace of matrix

In practice, an easy-to-use open-sourced tool, pytorch-fid [82], being the official implementation of FID using PyTorch, is adopted by this paper to compute FIDs of generated images. It is important to note that FID has a

negative correlation with the perceptual quality of generated samples; namely, the lower the value of FID, the better the model’s performance.

## 6. Experiments

Extensive experiments have been conducted to verify whether the proposed method is effective and logical. [Subsection 6.1](#) and [Subsection 6.2](#) detail the quantitative and qualitative comparison. [Subsection 6.3](#) analyses the powerful generative ability of PCDM. The results of ablation studies are reported in [Subsection 6.4](#).

### 6.1. Quantitative evaluation

[Table 1](#) compares the results obtained from our proposed PCDM, StructGAN and StructGAN-AE. It is important to note that StructGAN-SA-PT and StructGAN-AA-PT in [Table 1](#) are the top 2 methods proposed in StructGAN-AE. Except for FID, results of StructGAN and its variants come from the [Table 2](#) in StructGAN-AE. Based on the open-sourced code [38], StructGAN is re-trained to obtain FID, and all the hyperparameters are the default values in the original code. Because StructGAN-AE doesn’t open-source its code, there is no FID of StructGAN-AE in [Table 1](#). PCDM is trained on the Modified-dataset and is tested on the sub-dataset, respectively, to obtain the values of the metrics for 3 sub-datasets. As shown in [Table 1](#), the best  $Score_{IoU}$  and FID for each sub-dataset have been highlighted in bold.

**Table 1** Quantitative evaluation of the results obtained from different models.

Test set	Metrics	StructGAN [1]	StructGAN -SA-PT [3]	StructGAN -AA-PT [3]	<b>PCDM</b>	
<b>Group7-H1</b>	SIoU $\uparrow$	0.41	0.58	0.60	0.66	
	WIoU $\uparrow$	0.59	0.64	0.67	0.63	
	SWratio <sub>label</sub> = 0.41	SWratio <sub>pre</sub> $\uparrow$	0.50	0.53	0.48	0.42
	$\eta_{SWratio}$ $\uparrow$	80%	77%	81%	96.31%	
	$Score_{IoU}$ $\uparrow$	0.40	0.48	0.52	<b>0.62</b>	
	FID $\downarrow$	70.32	/	/	<b>21.05</b>	
<b>Group7-H2</b>	SIoU $\uparrow$	0.58	0.64	0.68	0.80	
	WIoU $\uparrow$	0.63	0.63	0.64	0.63	
	SWratio <sub>label</sub> = 0.58	SWratio <sub>pre</sub> $\uparrow$	0.66	0.63	0.72	0.58
	$\eta_{SWratio}$ $\uparrow$	86%	90%	81%	99.60%	
	$Score_{IoU}$ $\uparrow$	0.52	0.57	0.54	<b>0.71</b>	
	FID $\downarrow$	46.14	/	/	<b>24.29</b>	
<b>Group8</b>	SIoU $\uparrow$	0.74	0.80	0.78	1.07	
	WIoU $\uparrow$	0.72	0.74	0.71	0.69	
	SWratio <sub>label</sub> = 0.66	SWratio <sub>pre</sub> $\uparrow$	0.76	0.72	0.73	0.73
	$\eta_{SWratio}$ $\uparrow$	87%	91%	90%	90.59%	
	$Score_{IoU}$ $\uparrow$	0.65	0.70	0.67	<b>0.80</b>	
	FID $\downarrow$	43.47	/	/	<b>11.52</b>	

### 6.2. Qualitative comparison with StructGAN

This section lists the qualitative comparison results between PCDM and StructGAN, which are shown in [Fig. 6](#) below. It is important to note that the StructGAN is our retrained model based on the open-sourced code of StructGAN [76] and keep the same configuration because StructGAN doesn’t open-source the trained models.

Based on the visualization results, it is clear that the generation results of PCDM are closer to the manual labels and the wall boundaries are all horizontal and vertical

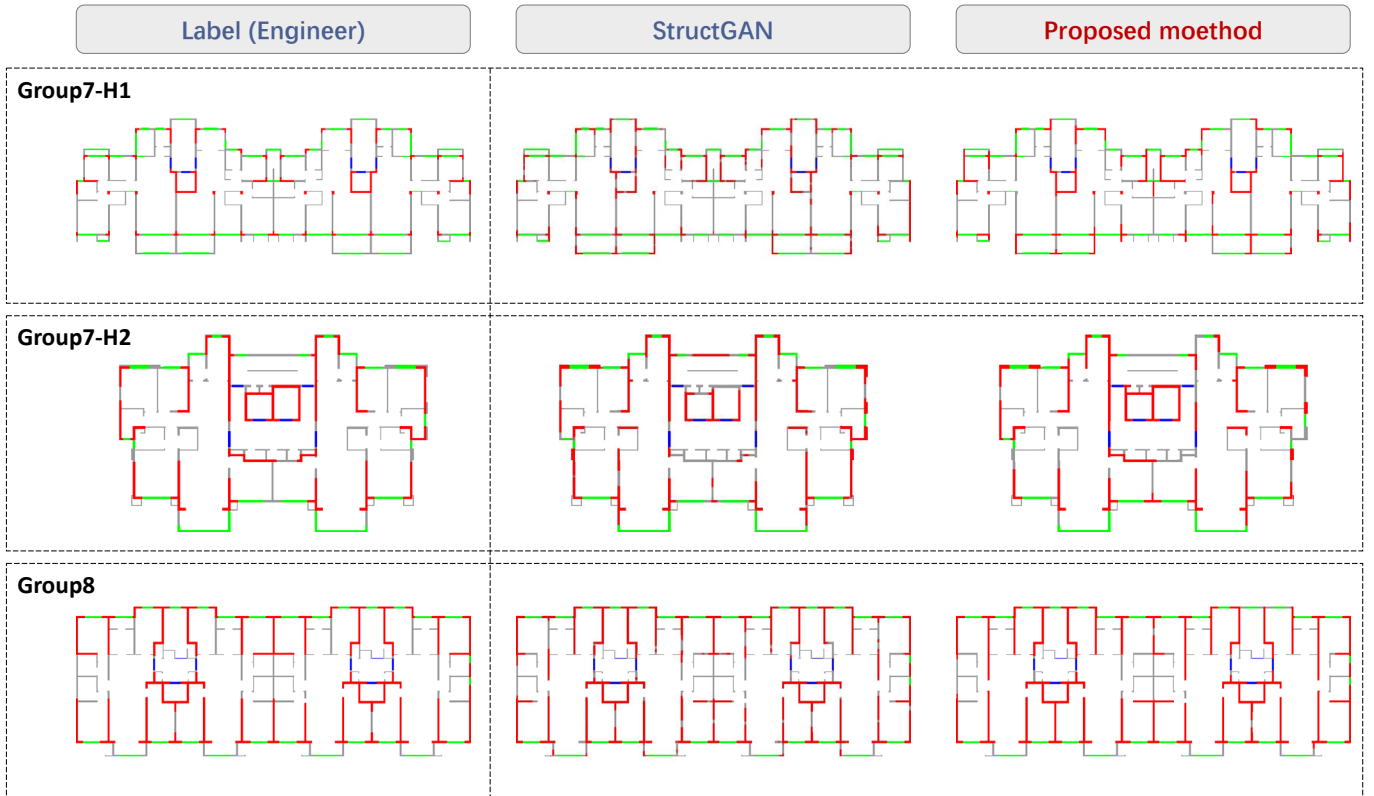


Fig. 6. Visualization comparison results.

### 6.3. Analysis of generative ability of PCDM

In this subsection, we analyze the generative ability of PCDM from two perspectives. The first aspect is that for the same input, we run the reverse denoising process multiple times to generate different designs based on the same model and ensure that the conditions match those in the label, which is in [Subsection 5.3.1](#). The second aspect is that for the same input, we input different physical conditions to make the model generate different results, which is in [Subsection 5.3.2](#).

#### 6.3.1. Generate different designs on a model

In this subsection, we run the sampling process repeatedly to make the model generate different designs. Some results are listed in [Fig. 7](#) below. It is clear that on the one hand, the generations are different every time, and on the other hand, the generations are close to labels. This shows that PCDM with power generation ability allows for diverse design.

#### 6.3.2. Generate different results meeting different conditions

In this subsection, we input different physical conditions and check if the model can generate different results meeting different conditions. As shown in [Fig. 7](#), the ground-truth physical condition of the first line images is 1.5, namely, the images belong to the Group7-H2 sub dataset, and the ground-truth physical condition of the second line images is 2.5, namely, the images belong to the Group8 sub dataset. When we input other physical conditions, it is clear that the model generate different results. Especially, the shear wall ratios of the images of the first column are significantly smaller than that of the images in the third column, which is consistent with the actual situations. However, on the other hand, we only train the model using the images with 1 physical condition, this is a new task

for PCDM, but PCDM can complete this task well. This shows that PCDM with power generation ability allows for creative design.

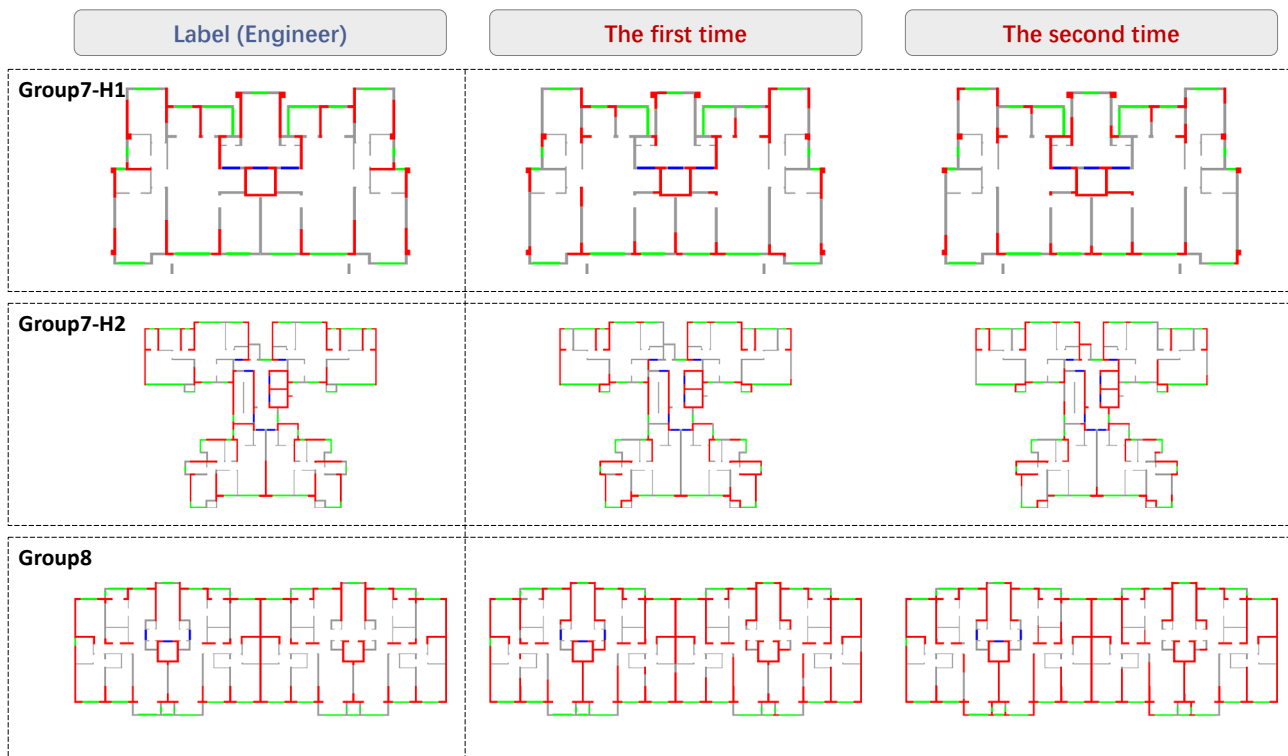


Fig. 7. Generate different designs based on a model.

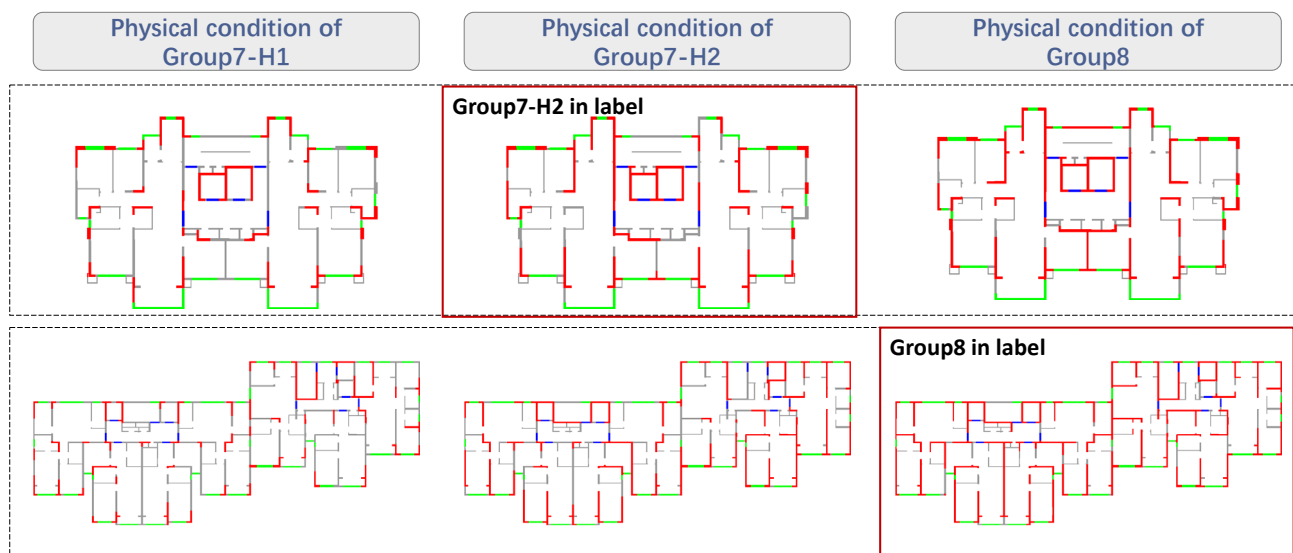


Fig. 8. Generate different results meeting different conditions.

#### 6.4. Ablation study

Ablation experiments are conducted to examine the validity of the designs, as delineated below.

##### 6.4.1. Predict $x_0$ or noise

As introduced before, this study predicts  $x_0$  rather than noise to focus on the similarity. Section 4 has analyzed the

theoretical equivalence and the actual effectiveness in ensuring the design similarity. To verify the actual effectiveness, this subsection conducts an ablation experiment to compare these two methods. As shown in Fig. 9, the results are more similar to the labels when the model predicts  $x_0$ , and they have the same background. When the model predicts noise, there is a significant difference between the results and the labels, which also confirms the analysis that estimating noise pays more attention to variability in Section 4.

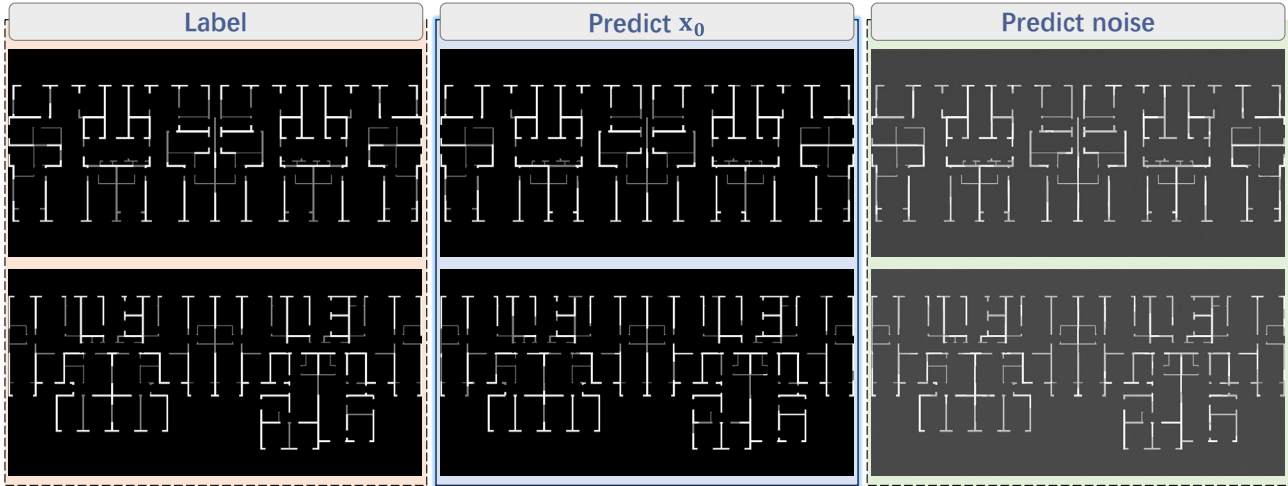


Fig. 9. Different prediction choices.

## 7. Conclusions

Intelligent structural design based on AI can resolve outstanding issues in structural design, for example, current structural design is always repetitive, inefficient, and time-consuming, and meet the growing needs of structural design. Thus, it has great potential to become the new design paradigm in the future, to assist and even replace human engineers, and has drawn extensive attention in both the academic and industrial communities. The current methods have limitations in many aspects to be addressed, such as application scope, visual quality of generated designs, or evaluation metrics of results. Therefore, this study introduces the most advanced AI tools and then proposes a comprehensive solution, which is detailed in the below paragraph. Besides, it is worth noting that all the implementation code of the proposed solution and the dataset used are available at <https://github.com/hzlbbfrog/Generative-BIM>.

Firstly, application scope. This paper introduces BIM into intelligent structural design and establishes a generative BIM structural design pipeline, which is a powerful supplement to the previous method only considering CAD drawings and also adapts to the needs of vigorously developing BIM technology in civil engineering. Then, three contributions are made to improve the perceptual quality and details of the generated images. (1) With respect to the generation framework, a 2-stage generative model-based generation framework is designed to reduce the difficulty of the design problem inspired by human painting. (2) With regard to the generative AI tools used, this study brings the latest DMs to the attention of the civil engineering community and replaces the original GAN-based models. Specifically, a novel physics-based conditional diffusion model, denoted as PCDM, is proposed to consider different physical conditions and ensure design similarity with the inputted architectural design drawings. This study revolves around the core idea of DMs and provides a clear and concise exposition of DMs to facilitate the understanding of the civil engineering community. Besides, many details and derivations that are omitted in many research papers are supplemented in the appendixes to help build a whole view of DMs. (3) With respect to the network structure, an attention block (AB) including a self-attention block (SAB) and a parallel cross-attention block (PCAB) is designed to facilitate the cross-domain fusion of image data and condition data. In addition, this study introduces the FID to quantitatively measure the perceptual quality of designed drawings to evaluate

generations synthetically.

Extensive experimental results elaborate the more powerful generation and representation capability of PCDM than GAN-based methods from the quantitative and qualitative aspects. Necessary ablation studies are also conducted to examine the validity of the proposed multiple designs.

Still, further studies are suggested in the following directions. In terms of the generation framework, inspired by the indirect regression-based method incorporating GNNs, GNNs can be introduced to combine with the indirect generative model-based framework proposed in this study to develop a graph-constrained and DM-based generation framework. The combination of prior graph knowledge and generative AI has the potential to generate more refined design drawings. In terms of the AI model, this study is still a primary and exploratory study about DMs, and the configuration is relatively basic. Better performance can be achieved if the model is fine-tuned further, *e.g.*, we can adopt a more advanced DM framework, such as score matching with Langevin dynamics (SMLD) [83][84], design more complicated CNN models or Transformer models, or embed more comprehensive and appropriate physical rules. In terms of the designed objects, this study pays attention to the intelligent design of shear wall structures limited by the dataset. Obviously, the proposed framework can be applied to the designs of other building types, such as steel structures and reinforced concrete frame structures, which is left to future work. Besides, in terms of application scope, the proposed generation framework based on DMs has the huge potential to replace GANs and become the new benchmark for other generative problems related to civil engineering, which is our future research focus.

### Declaration of competing interest

The authors declare that they have no known competing financial interests or personal relationships that could have appeared to influence the work reported in this paper.

### Acknowledgements

The research presented was financially supported by the Innovation Technology Fund, Midstream Research Programme for Universities [project no. MRP/003/21X], and the Hong Kong Research Grants Council [project no. 16205021]. The first author would like to sincerely thank Miss Shuqi Wei for drawing the two subgraphs in Fig. 3 (b). Authors would like to thank Dr. Wenjie Liao (the first author of StuctGAN) of THU for his valuable suggestions. The first author thanks Prof. Jack Cheng to teach him BIM in the course CIVL 5220-BIM and Digital Construction. The first author also thanks his group member Mr. Fangzhou Lin, Mr. Zhenyu Liang, Miss Yin Ni Lee, and Mr. Jeff Chan of HKUST for their help in the group project of CIVL 5220. The authors want to thank Dr. Cheng Ning Loong, Mr. Jimmy Wu, Mr. Tin Long Leung, Mr. Hao Xu, and Dr. Wai Yi Chau of HKUST for their valuable feedback. Finally, contributions by the anonymous reviewers are also highly appreciated.

## Appendix A Detailed derivation of formulas

### A.1 Derivation of Eq. (5)

Firstly, in Eq (4), we let  $\alpha_t = \frac{\bar{\alpha}_t}{\bar{\alpha}_{t-1}}$ , then

$$\beta_t = 1 - \alpha_t. \quad (\text{A1})$$

Plug (A1) into Eq. (1):

$$q(\mathbf{x}_t | \mathbf{x}_{t-1}) \triangleq \mathcal{N}(\mathbf{x}_t; \sqrt{\alpha_t} \mathbf{x}_{t-1}, (1 - \alpha_t) \mathbf{I}_D). \quad (\text{A2})$$

Using the reparameterization trick,  $\mathbf{x}_t$  can be expressed as

$$\mathbf{x}_t = \sqrt{\alpha_t} \mathbf{x}_{t-1} + \sqrt{1 - \alpha_t} \boldsymbol{\epsilon}_{t-1}. \quad (\text{A3})$$



Let  $t$  be  $t - 1$ :

$$\mathbf{x}_{t-1} = \sqrt{\alpha_{t-1}}\mathbf{x}_{t-2} + \sqrt{1 - \alpha_{t-1}}\boldsymbol{\epsilon}_{t-2}, \quad (\text{A4})$$

where  $\boldsymbol{\epsilon}_{t-1} \sim \mathcal{N}(0, \mathbf{I}_D)$  and  $\boldsymbol{\epsilon}_{t-2} \sim \mathcal{N}(0, \mathbf{I}_D)$ . Plug (A4) into (A3):

$$\mathbf{x}_t = \sqrt{\alpha_t}\sqrt{\alpha_{t-1}}\mathbf{x}_{t-2} + \sqrt{\alpha_t}\sqrt{1 - \alpha_{t-1}}\boldsymbol{\epsilon}_{t-2} + \sqrt{1 - \alpha_t}\boldsymbol{\epsilon}_{t-1}. \quad (\text{A5})$$

Based on the property of the Gaussian distribution, we know that the combination of 2 Gaussian distributions  $\sqrt{\alpha_t}\sqrt{1 - \alpha_{t-1}}\boldsymbol{\epsilon}_{t-2} + \sqrt{1 - \alpha_t}\boldsymbol{\epsilon}_{t-1}$  is also a Gaussian distribution:

$$\sqrt{\alpha_t}\sqrt{1 - \alpha_{t-1}}\boldsymbol{\epsilon}_{t-2} + \sqrt{1 - \alpha_t}\boldsymbol{\epsilon}_{t-1} \sim \mathcal{N}(0, (1 - \alpha_t\alpha_{t-1})\mathbf{I}_D). \quad (\text{A6})$$

Then, apply the reparameterization trick again:

$$\sqrt{\alpha_t}\sqrt{1 - \alpha_{t-1}}\boldsymbol{\epsilon}_{t-2} + \sqrt{1 - \alpha_t}\boldsymbol{\epsilon}_{t-1} = \sqrt{1 - \alpha_t\alpha_{t-1}}\boldsymbol{\epsilon}'_{t-2}, \quad (\text{A7})$$

where  $\boldsymbol{\epsilon}'_{t-2} \sim \mathcal{N}(0, \mathbf{I}_D)$ . Combine (A7) and (A5):

$$\mathbf{x}_t = \sqrt{\alpha_t\alpha_{t-1}}\mathbf{x}_{t-2} + \sqrt{1 - \alpha_t\alpha_{t-1}}\boldsymbol{\epsilon}'_{t-2}. \quad (\text{A8})$$

By analyzing (A8) and (A3), we can easily infer

$$\mathbf{x}_t = \sqrt{\alpha_t\alpha_{t-1}\cdots\alpha_1}\mathbf{x}_0 + \sqrt{1 - \alpha_t\alpha_{t-1}\cdots\alpha_1}\boldsymbol{\epsilon}'_0 = \sqrt{\prod_{i=1}^t \alpha_i}\mathbf{x}_0 + \sqrt{1 - \prod_{i=1}^t \alpha_i}\boldsymbol{\epsilon}'_0, \quad (\text{A9})$$

where  $\boldsymbol{\epsilon}'_0 \sim \mathcal{N}(0, \mathbf{I}_D)$ .

Based on the definition of  $\bar{\alpha}_t$  (see Eq (3)), we can expand  $t \in \{1, \dots, T\}$  to  $t = 0$ :

$$\bar{\alpha}_0 = \frac{g(0)}{g(0)} = 1. \quad (\text{A10})$$

Because of  $\alpha_t = \frac{\bar{\alpha}_t}{\bar{\alpha}_{t-1}}$ , for  $t \in \{1, \dots, T\}$ , we can obtain

$$\bar{\alpha}_t = \prod_{i=1}^t \alpha_i. \quad (\text{A11})$$

Embed (A11) into (A9) to simplify (A9):

$$\mathbf{x}_t = \sqrt{\bar{\alpha}_t}\mathbf{x}_0 + \sqrt{1 - \bar{\alpha}_t}\boldsymbol{\epsilon}, \quad (\text{A12})$$

where  $\boldsymbol{\epsilon} \sim \mathcal{N}(0, \mathbf{I}_D)$ . Then we can also get

$$q(\mathbf{x}_t | \mathbf{x}_0) = \mathcal{N}(\mathbf{x}_t; \sqrt{\bar{\alpha}_t}\mathbf{x}_0, (1 - \bar{\alpha}_t)\mathbf{I}_D). \quad (\text{A13})$$

## A.2 Derivation of Eqs. (7), (8), and (9)

Before introducing the derivation, a key theorem is proved first.

**Theorem 1.** For any probability density functions (pdfs), if they have the shape like

$$q(x) \propto \exp(-Ax^2 + Bx + C), A > 0,$$

the pdfs are Gaussian distributions.

*Proof.* First of all, we can add a coefficient  $D$  to replace the  $\propto$ :

$$q(x) = D \times \exp(-Ax^2 + Bx + C), A > 0. \quad (\text{A14})$$

Then, we transform the above formula Through some operations:

$$\begin{aligned} q(x) &= D \times \exp(-Ax^2 + Bx + C) \\ &= D \times \exp\left[-A\left(x^2 - \frac{B}{A}x - \frac{C}{A}\right)\right] \\ &= D \times \exp\left[-A\left(\left(x - \frac{B}{2A}\right)^2 - \frac{B^2}{4A^2} - \frac{C}{A}\right)\right] \end{aligned}$$

$$\begin{aligned}
 &= D \times \exp \left[ -A \left( x - \frac{B}{2A} \right)^2 + \frac{B^2 + 4AC}{4A} \right] \\
 &= D \times \exp \left( \frac{B^2 + 4AC}{4A} \right) \exp \left[ - \left( \sqrt{A} \left( x - \frac{B}{2A} \right) \right)^2 \right].
 \end{aligned} \tag{A15}$$

Further, according to the property of pdfs, we know that  $\int_{\mathbb{R}} q(x) dx = 1$ , so

$$\begin{aligned}
 \int_{\mathbb{R}} q(x) dx &= \int_{\mathbb{R}} D \times \exp \left( \frac{B^2 + 4AC}{4A} \right) \exp \left[ - \left( \sqrt{A} \left( x - \frac{B}{2A} \right) \right)^2 \right] dx \\
 &= D \times \exp \left( \frac{B^2 + 4AC}{4A} \right) \int_{\mathbb{R}} \exp \left[ - \left( \sqrt{A} \left( x - \frac{B}{2A} \right) \right)^2 \right] dx.
 \end{aligned} \tag{A16}$$

Then, we let  $h = \sqrt{A} \left( x - \frac{B}{2A} \right)$ . Therefore, we have  $x = \frac{\sqrt{A}}{A} h + \frac{B}{2A}$ , in other words,  $dx = \frac{\sqrt{A}}{A} dh$ . Next, substitute  $x$  in the above equation with  $h$  to simplify the formula:

$$\int_{\mathbb{R}} q(x) dx = D \times \exp \left( \frac{B^2 + 4AC}{4A} \right) \frac{\sqrt{A}}{A} \int_{\mathbb{R}} \exp(-h^2) dh. \tag{A17}$$

Next, we need to calculate the integral  $I = \int_{\mathbb{R}} \exp(-h^2) dh$ :

$$\begin{aligned}
 I \times I &= \left( \int_{\mathbb{R}} \exp(-x^2) dx \right) \times \left( \int_{\mathbb{R}} \exp(-y^2) dy \right) \\
 &= \int_{\mathbb{R}} \int_{\mathbb{R}} \exp[-(x^2 + y^2)] dx dy \\
 &= \int_0^{2\pi} \left( \int_0^{+\infty} r \exp[-(r^2)] dr \right) d\theta \\
 &= \int_0^{2\pi} \left( \int_0^{+\infty} \frac{1}{2} \exp[-u] du \right) d\theta \\
 &= \int_0^{2\pi} \frac{1}{2} d\theta \\
 &= \pi.
 \end{aligned} \tag{A18}$$

Therefore,  $I = \int_{\mathbb{R}} \exp(-h^2) dh = \sqrt{\pi}$ . Substitute  $\int_{\mathbb{R}} \exp(-h^2) dh$  in Eq. (A17) with  $\sqrt{\pi}$ :

$$\int_{\mathbb{R}} q(x) dx = D \times \exp \left( \frac{B^2 + 4AC}{4A} \right) \frac{\sqrt{A}}{A} \sqrt{\pi} = 1. \tag{A19}$$

So,

$$D \times \exp \left( \frac{B^2 + 4AC}{4A} \right) = \frac{\sqrt{A}}{\sqrt{\pi}}. \tag{A20}$$

Combining Eqs. (A15) and (A20), we have

$$q(x) = \frac{\sqrt{A}}{\sqrt{\pi}} \exp \left[ -A \left( x - \frac{B}{2A} \right)^2 \right]. \tag{A21}$$

Then, we let

$$A = \frac{1}{2\sigma^2}, \sigma > 0 \tag{A22}$$

and

$$\frac{B}{2A} = \mu, \quad (\text{A23})$$

Plug Eqs. (A22) and (A23) into Eq. (A21):

$$\begin{aligned} q(x) &= \frac{\sqrt{\frac{1}{2\sigma^2}}}{\sqrt{\pi}} \exp\left[-\frac{1}{2\sigma^2}(x - \mu)^2\right] \\ &= \frac{1}{\sqrt{2\pi}\sigma} \exp\left[-\frac{1}{2\sigma^2}(x - \mu)^2\right]. \end{aligned} \quad (\text{A24})$$

Obviously, Eq. (A21) is just the expression of the Gaussian distribution, where  $\mu$  is the mean,  $\sigma^2$  is the variance, and  $\sigma$  is named the standard deviation. So far, we have proved the Theorem 1.  $\square$

**Remark 1.** There are two points we should be aware of. (1) In the Theorem 1, we only consider the situation that  $x$  is a scalar. However, it can be easily extended to the situation that  $\mathbf{x}$  is a vector. Because the proof is similar to the proof of Theorem 1, for simplicity, we omit the proof but hold the conclusion. (2) Note that there is no  $C$  and  $D$  that are terms independent of  $x$  in Eq. (A21), and their functions is to make the integral of  $q(x)$  equal to (see Eqs. (A19) and (A20)) 1, which means we can neglect the terms not involving  $x$ , which doesn't affect the results. This is further clarified in the following derivation.

Then, let's start the derivation of Eqs. (7), (8), and (9). Based on the Eq. (10),  $q(\mathbf{x}_{t-1}|\mathbf{x}_t, \mathbf{x}_0)$  can be written as

$$\begin{aligned} q(\mathbf{x}_{t-1}|\mathbf{x}_t, \mathbf{x}_0) &= \frac{q(\mathbf{x}_t|\mathbf{x}_{t-1}, \mathbf{x}_0)q(\mathbf{x}_{t-1}|\mathbf{x}_0)}{q(\mathbf{x}_t|\mathbf{x}_0)} \\ &= \frac{q(\mathbf{x}_t|\mathbf{x}_{t-1})q(\mathbf{x}_{t-1}|\mathbf{x}_0)}{q(\mathbf{x}_t|\mathbf{x}_0)}. \end{aligned} \quad (\text{Markov Property}) \quad (\text{A25})$$

According to Eq. (1) and the property of the multivariate Gaussian distribution, we have

$$\begin{aligned} q(\mathbf{x}_t|\mathbf{x}_{t-1}) &= \frac{1}{(2\pi)^{D/2}|\beta_t \mathbf{I}_D|^{1/2}} \exp\left(-\frac{1}{2}(\mathbf{x}_t - \sqrt{1 - \beta_t} \mathbf{x}_{t-1})^\top (\beta_t \mathbf{I}_D)^{-1} (\mathbf{x}_t - \sqrt{1 - \beta_t} \mathbf{x}_{t-1})\right) \\ &\propto \exp\left(-\frac{1}{2} \frac{(\mathbf{x}_t - \sqrt{1 - \beta_t} \mathbf{x}_{t-1})^\top (\mathbf{x}_t - \sqrt{1 - \beta_t} \mathbf{x}_{t-1})}{\beta_t}\right). \end{aligned} \quad (\text{A26})$$

Correspondingly, based on Eq. (5), we can get

$$q(\mathbf{x}_t|\mathbf{x}_0) \propto \exp\left(-\frac{1}{2} \frac{(\mathbf{x}_t - \sqrt{\bar{\alpha}_t} \mathbf{x}_0)^\top (\mathbf{x}_t - \sqrt{\bar{\alpha}_t} \mathbf{x}_0)}{1 - \bar{\alpha}_t}\right), \quad (\text{A27})$$

and

$$q(\mathbf{x}_{t-1}|\mathbf{x}_0) \propto \exp\left(-\frac{1}{2} \frac{(\mathbf{x}_{t-1} - \sqrt{\bar{\alpha}_{t-1}} \mathbf{x}_0)^\top (\mathbf{x}_{t-1} - \sqrt{\bar{\alpha}_{t-1}} \mathbf{x}_0)}{1 - \bar{\alpha}_{t-1}}\right). \quad (\text{A28})$$

Plug Eqs. (A26), (A27), and (A28) into Eq. (A25):

$$\begin{aligned} q(\mathbf{x}_{t-1}|\mathbf{x}_t, \mathbf{x}_0) &\propto \exp\left[-\frac{1}{2} \left( \frac{(\mathbf{x}_t - \sqrt{1 - \beta_t} \mathbf{x}_{t-1})^\top (\mathbf{x}_t - \sqrt{1 - \beta_t} \mathbf{x}_{t-1})}{\beta_t} \right. \right. \\ &\quad \left. \left. + \frac{(\mathbf{x}_{t-1} - \sqrt{\bar{\alpha}_{t-1}} \mathbf{x}_0)^\top (\mathbf{x}_{t-1} - \sqrt{\bar{\alpha}_{t-1}} \mathbf{x}_0)}{1 - \bar{\alpha}_{t-1}} - \frac{(\mathbf{x}_t - \sqrt{\bar{\alpha}_t} \mathbf{x}_0)^\top (\mathbf{x}_t - \sqrt{\bar{\alpha}_t} \mathbf{x}_0)}{1 - \bar{\alpha}_t} \right) \right], \end{aligned} \quad (\text{A29})$$

Because the random vector here is  $\mathbf{X}_{t-1}$ , and we want to get the distribution of  $\mathbf{X}_{t-1}$ , namely,  $\mathbf{x}_{t-1}$  is the core object. Next, remove the innermost brackets related to  $\mathbf{x}_{t-1}$ :

$$q(\mathbf{x}_{t-1}|\mathbf{x}_t, \mathbf{x}_0) \propto \exp \left[ -\frac{1}{2} \left( \frac{\mathbf{x}_t^\top \mathbf{x}_t - \mathbf{x}_{t-1}^\top (2\sqrt{1-\beta_t} \mathbf{x}_t) + (1-\beta_t) \mathbf{x}_{t-1}^\top \mathbf{x}_{t-1}}{\beta_t} + \frac{\mathbf{x}_{t-1}^\top \mathbf{x}_{t-1} - \mathbf{x}_{t-1}^\top (2\sqrt{\bar{\alpha}_{t-1}} \mathbf{x}_0) + \bar{\alpha}_{t-1} \mathbf{x}_0^\top \mathbf{x}_0 - (\mathbf{x}_t - \sqrt{\bar{\alpha}_t} \mathbf{x}_0)^\top (\mathbf{x}_t - \sqrt{\bar{\alpha}_t} \mathbf{x}_0)}{1-\bar{\alpha}_{t-1}} - \frac{(\mathbf{x}_t - \sqrt{\bar{\alpha}_t} \mathbf{x}_0)^\top (\mathbf{x}_t - \sqrt{\bar{\alpha}_t} \mathbf{x}_0)}{1-\bar{\alpha}_t} \right) \right]. \quad (\text{A30})$$

Then, collect like terms based on  $\mathbf{x}_{t-1}$ :

$$\begin{aligned} & q(\mathbf{x}_{t-1}|\mathbf{x}_t, \mathbf{x}_0) \\ & \propto \exp \left[ -\frac{1}{2} \left( \left( \frac{1-\beta_t}{\beta_t} + \frac{1}{1-\bar{\alpha}_{t-1}} \right) \mathbf{x}_{t-1}^\top \mathbf{x}_{t-1} - \mathbf{x}_{t-1}^\top \left( \frac{2\sqrt{1-\beta_t} \mathbf{x}_t}{\beta_t} + \frac{2\sqrt{\bar{\alpha}_{t-1}} \mathbf{x}_0}{1-\bar{\alpha}_{t-1}} \right) + C_0(\mathbf{x}_t, \mathbf{x}_0) \right) \right] \\ & = \exp \left[ -\frac{1}{2} \left( \mathbf{x}_{t-1}^\top \left( \frac{1-\beta_t}{\beta_t} + \frac{1}{1-\bar{\alpha}_{t-1}} \right) \mathbf{x}_{t-1} - \mathbf{x}_{t-1}^\top \left( \frac{2\sqrt{1-\beta_t} \mathbf{x}_t}{\beta_t} + \frac{2\sqrt{\bar{\alpha}_{t-1}} \mathbf{x}_0}{1-\bar{\alpha}_{t-1}} \right) \right) \right]. \end{aligned} \quad (\text{A31})$$

where  $C_0(\mathbf{x}_t, \mathbf{x}_0)$  doesn't involve  $\mathbf{x}_{t-1}$ , and its function is to let the integral of the pdf be 1. Recall the Remark 1, it is clear that we can represent  $q(\mathbf{x}_{t-1}|\mathbf{x}_t, \mathbf{x}_0)$  without knowing the specific expression of  $C_0(\mathbf{x}_t, \mathbf{x}_0)$ , so omit this term.

Because the exponent term of the pdf is a quadratic polynomial of  $\mathbf{x}_{t-1}$ , the unique distribution satisfying this is Gaussian distributions based on the Theorem 1. Thus,  $q(\mathbf{x}_{t-1}|\mathbf{x}_t, \mathbf{x}_0)$  can be modeled as follows:

$$q(\mathbf{x}_{t-1}|\mathbf{x}_t, \mathbf{x}_0) = \mathcal{N} \left( \mathbf{x}_{t-1}; \tilde{\boldsymbol{\mu}}_t(\mathbf{x}_t, \mathbf{x}_0), \tilde{\boldsymbol{\Sigma}}_t(\mathbf{x}_t, \mathbf{x}_0) \right), \quad (\text{A32})$$

where  $\tilde{\boldsymbol{\mu}}_t(\mathbf{x}_t, \mathbf{x}_0)$  is the mean vector, and  $\tilde{\boldsymbol{\Sigma}}_t(\mathbf{x}_t, \mathbf{x}_0)$  is the covariance matrix. Based on the property of the multivariate Gaussian distribution, Eq. (A32) can be written as

$$\begin{aligned} q(\mathbf{x}_{t-1}|\mathbf{x}_t, \mathbf{x}_0) & \propto \exp \left( -\frac{1}{2} (\mathbf{x}_{t-1} - \tilde{\boldsymbol{\mu}}_t(\mathbf{x}_t, \mathbf{x}_0))^\top \left( \tilde{\boldsymbol{\Sigma}}_t(\mathbf{x}_t, \mathbf{x}_0) \right)^{-1} (\mathbf{x}_{t-1} - \tilde{\boldsymbol{\mu}}_t(\mathbf{x}_t, \mathbf{x}_0)) \right) \\ & = \exp \left( -\frac{1}{2} (\mathbf{x}_{t-1}^\top \tilde{\boldsymbol{\Sigma}}_t^{-1} - \tilde{\boldsymbol{\mu}}_t^\top \tilde{\boldsymbol{\Sigma}}_t^{-1}) (\mathbf{x}_{t-1} - \tilde{\boldsymbol{\mu}}_t) \right) \\ & = \exp \left( -\frac{1}{2} (\mathbf{x}_{t-1}^\top \tilde{\boldsymbol{\Sigma}}_t^{-1} \mathbf{x}_{t-1} - \mathbf{x}_{t-1}^\top \tilde{\boldsymbol{\Sigma}}_t^{-1} \tilde{\boldsymbol{\mu}}_t - \tilde{\boldsymbol{\mu}}_t^\top \tilde{\boldsymbol{\Sigma}}_t^{-1} \mathbf{x}_{t-1} + \tilde{\boldsymbol{\mu}}_t^\top \tilde{\boldsymbol{\Sigma}}_t^{-1} \tilde{\boldsymbol{\mu}}_t) \right). \end{aligned} \quad (\text{A33})$$

Because  $\tilde{\boldsymbol{\mu}}_t^\top \tilde{\boldsymbol{\Sigma}}_t^{-1} \mathbf{x}_{t-1}$  is a scalar,  $\tilde{\boldsymbol{\mu}}_t^\top \tilde{\boldsymbol{\Sigma}}_t^{-1} \mathbf{x}_{t-1} = (\tilde{\boldsymbol{\mu}}_t^\top \tilde{\boldsymbol{\Sigma}}_t^{-1} \mathbf{x}_{t-1})^\top = \mathbf{x}_{t-1}^\top (\tilde{\boldsymbol{\Sigma}}_t^{-1})^\top \tilde{\boldsymbol{\mu}}_t$ . Further,  $\tilde{\boldsymbol{\Sigma}}_t$  is symmetric, so  $\tilde{\boldsymbol{\Sigma}}_t^{-1}$  is symmetric. Then we have  $\tilde{\boldsymbol{\Sigma}}_t^{-1} = (\tilde{\boldsymbol{\Sigma}}_t^{-1})^\top$ , namely,  $\tilde{\boldsymbol{\mu}}_t^\top \tilde{\boldsymbol{\Sigma}}_t^{-1} \mathbf{x}_{t-1} = \mathbf{x}_{t-1}^\top \tilde{\boldsymbol{\Sigma}}_t^{-1} \tilde{\boldsymbol{\mu}}_t$ . Plug this equation into Eq. (A33):

$$\begin{aligned} q(\mathbf{x}_{t-1}|\mathbf{x}_t, \mathbf{x}_0) & \propto \exp \left( -\frac{1}{2} (\mathbf{x}_{t-1}^\top \tilde{\boldsymbol{\Sigma}}_t^{-1} \mathbf{x}_{t-1} - 2\mathbf{x}_{t-1}^\top \tilde{\boldsymbol{\Sigma}}_t^{-1} \tilde{\boldsymbol{\mu}}_t + C_1(\mathbf{x}_t, \mathbf{x}_0)) \right) \\ & \propto \exp \left( -\frac{1}{2} (\mathbf{x}_{t-1}^\top \tilde{\boldsymbol{\Sigma}}_t^{-1} \mathbf{x}_{t-1} - \mathbf{x}_{t-1}^\top (2\tilde{\boldsymbol{\Sigma}}_t^{-1} \tilde{\boldsymbol{\mu}}_t)) \right), \end{aligned} \quad (\text{A34})$$

where  $C_1(\mathbf{x}_t, \mathbf{x}_0)$  denotes terms which are independent of  $\mathbf{x}_{t-1}$ . Recall the Remark 1, we also omit  $C_1(\mathbf{x}_t, \mathbf{x}_0)$  here just like Eq. (A31) does. It is clear that  $C_0(\mathbf{x}_t, \mathbf{x}_0) = C_1(\mathbf{x}_t, \mathbf{x}_0)$ . Then, things become very easy. Combining

Eqs. (A31) and (A34), we can establish 2 equations containing  $\tilde{\boldsymbol{\mu}}_t$  and  $\tilde{\boldsymbol{\Sigma}}_t$  by the method of undetermined coefficients:

$$\begin{cases} \tilde{\boldsymbol{\Sigma}}_t^{-1} = \frac{1 - \beta_t}{\beta_t} + \frac{1}{1 - \bar{\alpha}_{t-1}} \\ 2\tilde{\boldsymbol{\Sigma}}_t^{-1}\tilde{\boldsymbol{\mu}}_t = \frac{2\sqrt{1 - \beta_t}\mathbf{x}_t}{\beta_t} + \frac{2\sqrt{\bar{\alpha}_{t-1}}\mathbf{x}_0}{1 - \bar{\alpha}_{t-1}} \end{cases} \quad (\text{A35})$$

Obviously,  $\tilde{\boldsymbol{\mu}}_t$  and  $\tilde{\boldsymbol{\Sigma}}_t$  can be derived from the above two equations.

let's firstly derive  $\tilde{\boldsymbol{\Sigma}}_t$  by the first equation in Eq. (A35). Because  $\tilde{\boldsymbol{\Sigma}}_t^{-1} \in \mathbb{R}^{D \times D}$  and the right-hand side of the first equation is a scalar, the first equation can be transformed into a strict form:

$$\tilde{\boldsymbol{\Sigma}}_t^{-1} = \left( \frac{1 - \beta_t}{\beta_t} + \frac{1}{1 - \bar{\alpha}_{t-1}} \right) \mathbf{I}_D. \quad (\text{A36})$$

Then, we can obtain  $\tilde{\boldsymbol{\Sigma}}_t$ :

$$\begin{aligned} \tilde{\boldsymbol{\Sigma}}_t &= 1 / \left( \frac{1 - \beta_t}{\beta_t} + \frac{1}{1 - \bar{\alpha}_{t-1}} \right) \mathbf{I}_D \\ &= 1 / \frac{(1 - \beta_t)(1 - \bar{\alpha}_{t-1}) + \beta_t}{\beta_t(1 - \bar{\alpha}_{t-1})} \mathbf{I}_D \\ &= \frac{\beta_t(1 - \bar{\alpha}_{t-1})}{1 - \bar{\alpha}_{t-1} - \beta_t + \beta_t\bar{\alpha}_{t-1} + \beta_t} \mathbf{I}_D \\ &= \frac{\beta_t(1 - \bar{\alpha}_{t-1})}{1 - \bar{\alpha}_{t-1} + \beta_t\bar{\alpha}_{t-1}} \mathbf{I}_D. \end{aligned} \quad (\text{A37})$$

Recall Eq. (4):

$$\beta_t = 1 - \frac{\bar{\alpha}_t}{\bar{\alpha}_{t-1}}. \quad (\text{A38})$$

namely,

$$\beta_t\bar{\alpha}_{t-1} = \bar{\alpha}_{t-1} - \bar{\alpha}_t. \quad (\text{A39})$$

We can obtain  $\tilde{\boldsymbol{\Sigma}}_t$  after plugging Eq. (A39) into Eq. (A37):

$$\tilde{\boldsymbol{\Sigma}}_t = \frac{1 - \bar{\alpha}_{t-1}}{1 - \bar{\alpha}_t} \beta_t \mathbf{I}_D. \quad (\text{A40})$$

Further, we can think of  $\frac{1 - \bar{\alpha}_{t-1}}{1 - \bar{\alpha}_t} \beta_t$  as a product of  $\beta_t$  and a coefficient, so we let  $\tilde{\beta}_t = \frac{1 - \bar{\alpha}_{t-1}}{1 - \bar{\alpha}_t} \beta_t$ , and  $\tilde{\boldsymbol{\Sigma}}_t = \tilde{\beta}_t \mathbf{I}_D$ .

Next, let's derive  $\tilde{\boldsymbol{\mu}}_t$ . Firstly, simplify the second equation of Eq. (A35):

$$\tilde{\boldsymbol{\mu}}_t = \tilde{\boldsymbol{\Sigma}}_t \left( \frac{\sqrt{1 - \beta_t}\mathbf{x}_t}{\beta_t} + \frac{\sqrt{\bar{\alpha}_{t-1}}\mathbf{x}_0}{1 - \bar{\alpha}_{t-1}} \right). \quad (\text{A41})$$

Substitute  $\tilde{\boldsymbol{\Sigma}}_t$  with Eq. (A40):

$$\begin{aligned} \tilde{\boldsymbol{\mu}}_t &= \frac{1 - \bar{\alpha}_{t-1}}{1 - \bar{\alpha}_t} \beta_t \mathbf{I}_D \left( \frac{\sqrt{1 - \beta_t}\mathbf{x}_t}{\beta_t} + \frac{\sqrt{\bar{\alpha}_{t-1}}\mathbf{x}_0}{1 - \bar{\alpha}_{t-1}} \right) \\ &= \frac{\sqrt{1 - \beta_t}\mathbf{x}_t}{\beta_t} \frac{1 - \bar{\alpha}_{t-1}}{1 - \bar{\alpha}_t} \beta_t + \frac{\sqrt{\bar{\alpha}_{t-1}}\mathbf{x}_0}{1 - \bar{\alpha}_{t-1}} \frac{1 - \bar{\alpha}_{t-1}}{1 - \bar{\alpha}_t} \beta_t \\ &= \frac{\sqrt{1 - \beta_t}(1 - \bar{\alpha}_{t-1})}{1 - \bar{\alpha}_t} \mathbf{x}_t + \frac{\sqrt{\bar{\alpha}_{t-1}}\beta_t}{1 - \bar{\alpha}_t} \mathbf{x}_0. \end{aligned} \quad (\text{A42})$$

So far, the derivation of Eqs. (7), (8), and (9) have been completed.

### A.3 Derivation of Eq. (16)

Firstly, change the form of Eq. (6):

$$\mathbf{x}_0 = \frac{1}{\sqrt{\alpha_t}} (\mathbf{x}_t - \sqrt{1 - \bar{\alpha}_t} \epsilon). \quad (\text{A43})$$

Plug the above equation into Eq. (8):

$$\begin{aligned} \tilde{\boldsymbol{\mu}}_t(\mathbf{x}_t, \mathbf{x}_0) &= \frac{\sqrt{1 - \beta_t}(1 - \bar{\alpha}_{t-1})}{1 - \bar{\alpha}_t} \mathbf{x}_t + \frac{\sqrt{\bar{\alpha}_{t-1}}\beta_t}{1 - \bar{\alpha}_t} \mathbf{x}_0 \\ &= \frac{\sqrt{1 - \beta_t}(1 - \bar{\alpha}_{t-1})}{1 - \bar{\alpha}_t} \mathbf{x}_t + \frac{\sqrt{\bar{\alpha}_{t-1}}\beta_t}{1 - \bar{\alpha}_t} \times \frac{\mathbf{x}_t - \sqrt{1 - \bar{\alpha}_t} \epsilon}{\sqrt{\bar{\alpha}_t}} \\ &= \left( \frac{\sqrt{\alpha_t}(1 - \bar{\alpha}_{t-1})}{1 - \bar{\alpha}_t} + \frac{\beta_t}{(1 - \bar{\alpha}_t)\sqrt{\alpha_t}} \right) \mathbf{x}_t - \frac{\beta_t}{\sqrt{1 - \bar{\alpha}_t}} \times \frac{\epsilon}{\sqrt{\alpha_t}} \\ &= \left( \frac{\alpha_t(1 - \bar{\alpha}_{t-1}) + 1 - \alpha_t}{(1 - \bar{\alpha}_t)\sqrt{\alpha_t}} \right) \mathbf{x}_t - \frac{1}{\sqrt{\alpha_t}} \frac{\beta_t}{\sqrt{1 - \bar{\alpha}_t}} \epsilon \\ &= \frac{1 - \alpha_t \bar{\alpha}_{t-1}}{(1 - \bar{\alpha}_t)\sqrt{\alpha_t}} \mathbf{x}_t - \frac{1}{\sqrt{\alpha_t}} \frac{\beta_t}{\sqrt{1 - \bar{\alpha}_t}} \epsilon \\ &= \frac{1}{\sqrt{\alpha_t}} \left( \mathbf{x}_t - \frac{1 - \alpha_t}{\sqrt{1 - \bar{\alpha}_t}} \epsilon \right). \end{aligned} \quad (\text{A44})$$

Besides,  $\alpha_t$  can be replaced by  $1 - \beta_t$ :

$$\tilde{\boldsymbol{\mu}}_t(\mathbf{x}_t, \mathbf{x}_0) = \frac{1}{\sqrt{1 - \beta_t}} \left( \mathbf{x}_t - \frac{\beta_t}{\sqrt{1 - \bar{\alpha}_t}} \epsilon \right). \quad (\text{A45})$$

## Appendix B Proof of the optimization process

In [Subsection 4.4](#), we get  $q(\mathbf{x}_{t-1} | \mathbf{x}_t, \mathbf{x}_0) = \mathcal{N}(\mathbf{x}_{t-1}; \tilde{\boldsymbol{\mu}}_t(\mathbf{x}_t, \mathbf{x}_0), \tilde{\boldsymbol{\Sigma}}_t)$ . In [Subsection 4.5](#), we know that

$p_{\theta}(\mathbf{x}_{t-1} | \mathbf{x}_t, \mathbf{y}, d) = \mathcal{N}(\mathbf{x}_{t-1}; \boldsymbol{\mu}_{\theta}(\mathbf{x}_t, t, \mathbf{y}, d), \boldsymbol{\Sigma}_{\theta}(\mathbf{x}_t, t, \mathbf{y}, d))$ , where  $\boldsymbol{\Sigma}_{\theta}(\mathbf{x}_t, t, \mathbf{y}, d)$  is set to  $\tilde{\boldsymbol{\Sigma}}_t$ . In this section, we first want to proof the relationship between minimizing the loss function in Eq. (12), denoted as  $\mathcal{L}_1$ , and optimizing  $p_{\theta}(\mathbf{x}_{t-1} | \mathbf{x}_t, \mathbf{y}, d)$  to make it close to  $q(\mathbf{x}_{t-1} | \mathbf{x}_t, \mathbf{x}_0)$ .

The first thing is to use an appropriate mathematical tool to represent the proximity between two distributions, namely, quantify the distance. In machine learning, Kullback-Leibler divergence or KL divergence is the most widely used metric to measure the distance between two distributions. Specifically, the smaller of the KL divergence, the “*closer*” or “*more similar*” the two distributions are. The KL divergence can be defined by the following equation:

$$D_{\text{KL}}(P \parallel Q) \triangleq \int_{\mathcal{X}} P(x) \log \frac{P(x)}{Q(x)} dx, \quad (\text{B1})$$

where  $D_{\text{KL}}$  is the KL divergence,  $P$  and  $Q$  are two arbitrary continuous distributions, and  $\mathcal{X}$  denotes the sample space. The KL divergence is also known as the information gain or the relative entropy [85].

Because the distributions  $p_{\theta}$  and  $q$  researched here are both multivariate Gaussian distributions, we give the next simple proposition without proof to show the KL divergence between two multivariate Gaussian distributions:

**Proposition 1.** The KL divergence between two multivariate Gaussian distributions is

$$D_{\text{KL}}(\mathcal{N}(\mathbf{x}; \boldsymbol{\mu}_1, \boldsymbol{\Sigma}_1) \parallel \mathcal{N}(\mathbf{y}; \boldsymbol{\mu}_2, \boldsymbol{\Sigma}_2)) = \frac{1}{2} \left[ \text{Tr}(\boldsymbol{\Sigma}_2^{-1} \boldsymbol{\Sigma}_1) + (\boldsymbol{\mu}_2 - \boldsymbol{\mu}_1)^{\top} \boldsymbol{\Sigma}_2^{-1} (\boldsymbol{\mu}_2 - \boldsymbol{\mu}_1) - D + \log \frac{|\boldsymbol{\Sigma}_2|}{|\boldsymbol{\Sigma}_1|} \right], \quad (\text{B2})$$

where  $(\boldsymbol{\mu}_1, \boldsymbol{\Sigma}_1)$  and  $(\boldsymbol{\mu}_2, \boldsymbol{\Sigma}_2)$  represent the mean vectors and covariance matrices of the two distributions,

respectively.  $D$  means the dimension of the two random vectors,  $\mathbf{X}$  and  $\mathbf{Y}$ .

Then, a key theorem is given and proved.

**Theorem 2.** Minimizing the loss function  $\mathcal{L}_1$  is equivalent to making  $p_\theta(\mathbf{x}_{t-1}|\mathbf{x}_t, \mathbf{y}, d)$  close to  $q(\mathbf{x}_{t-1}|\mathbf{x}_t, \mathbf{x}_0)$ .

*Proof.* Since we have  $p_\theta(\mathbf{x}_{t-1}|\mathbf{x}_t, \mathbf{y}, d) = \mathcal{N}(\mathbf{x}_{t-1}; \boldsymbol{\mu}_\theta(\mathbf{x}_t, t, \mathbf{y}, d), \widetilde{\boldsymbol{\Sigma}}_t)$  and  $q(\mathbf{x}_{t-1}|\mathbf{x}_t, \mathbf{x}_0) = \mathcal{N}(\mathbf{x}_{t-1}; \tilde{\boldsymbol{\mu}}_t(\mathbf{x}_t, \mathbf{x}_0), \widetilde{\boldsymbol{\Sigma}}_t)$ , plug them into Eq. (B2) in the Proposition 1:

$$\begin{aligned} & D_{\text{KL}}(p_\theta(\mathbf{x}_{t-1}|\mathbf{x}_t, \mathbf{y}, d) \parallel q(\mathbf{x}_{t-1}|\mathbf{x}_t, \mathbf{x}_0)) \\ &= D_{\text{KL}}\left(\mathcal{N}(\mathbf{x}_{t-1}; \boldsymbol{\mu}_\theta(\mathbf{x}_t, t, \mathbf{y}, d), \widetilde{\boldsymbol{\Sigma}}_t) \parallel \mathcal{N}(\mathbf{x}_{t-1}; \tilde{\boldsymbol{\mu}}_t(\mathbf{x}_t, \mathbf{x}_0), \widetilde{\boldsymbol{\Sigma}}_t)\right) \\ &= \frac{1}{2} \left[ \text{Tr}(\widetilde{\boldsymbol{\Sigma}}_t^{-1} \widetilde{\boldsymbol{\Sigma}}_t) + (\tilde{\boldsymbol{\mu}}_t - \boldsymbol{\mu}_\theta)^\top \widetilde{\boldsymbol{\Sigma}}_t^{-1} (\tilde{\boldsymbol{\mu}}_t - \boldsymbol{\mu}_\theta) - D + \log \frac{|\widetilde{\boldsymbol{\Sigma}}_t|}{|\widetilde{\boldsymbol{\Sigma}}_t|} \right]. \end{aligned} \quad (\text{B3})$$

Further, by Subsection 4.4, we know that is  $p_\theta$  and  $q$  are isotropic Gaussian distributions, and  $\widetilde{\boldsymbol{\Sigma}}_t = \tilde{\beta}_t \mathbf{I}_D$ . So  $\widetilde{\boldsymbol{\Sigma}}_t^{-1} = \tilde{\beta}_t^{-1} \mathbf{I}_D$ . Plug the two equations into Eq. (B3):

$$\begin{aligned} & D_{\text{KL}}(p_\theta(\mathbf{x}_{t-1}|\mathbf{x}_t, \mathbf{y}, d) \parallel q(\mathbf{x}_{t-1}|\mathbf{x}_t, \mathbf{x}_0)) \\ &= \frac{1}{2} \left[ \text{Tr}(\tilde{\beta}_t^{-1} \mathbf{I}_D \tilde{\beta}_t \mathbf{I}_D) + (\tilde{\boldsymbol{\mu}}_t - \boldsymbol{\mu}_\theta)^\top \tilde{\beta}_t^{-1} \mathbf{I}_D (\tilde{\boldsymbol{\mu}}_t - \boldsymbol{\mu}_\theta) - D + \log 1 \right] \\ &= \frac{1}{2} \left[ \text{Tr}(\mathbf{I}_D) + \tilde{\beta}_t^{-1} (\tilde{\boldsymbol{\mu}}_t - \boldsymbol{\mu}_\theta)^\top (\tilde{\boldsymbol{\mu}}_t - \boldsymbol{\mu}_\theta) - D \right] \\ &= \frac{1}{2} \left[ D + \tilde{\beta}_t^{-1} \|\tilde{\boldsymbol{\mu}}_t - \boldsymbol{\mu}_\theta\|^2 - D \right] \\ &= \frac{1}{2\tilde{\beta}_t} \left[ \|\tilde{\boldsymbol{\mu}}_t - \boldsymbol{\mu}_\theta\|^2 \right]. \end{aligned} \quad (\text{B4})$$

Recall Eq. (12):

$$\mathcal{L} = \mathbb{E}_{t \sim \text{Uniform}[1, T], \mathbf{x}_0, \epsilon \sim \mathcal{N}(0, \mathbf{I}_D)} \|\tilde{\boldsymbol{\mu}}_t - \boldsymbol{\mu}_\theta(\mathbf{x}_t, t, \mathbf{y}, d)\|_2^2, \quad (\text{B5})$$

and  $\tilde{\beta}_t = \frac{1 - \bar{\alpha}_t}{1 - \bar{\alpha}_t} \beta_t > 0$ . Therefore,

$$\min_{\theta} \mathcal{L} \iff \min_{\theta} \|\tilde{\boldsymbol{\mu}}_t - \boldsymbol{\mu}_\theta(\mathbf{x}_t, t, \mathbf{y}, d)\|_2^2 \iff \min_{\theta} \frac{1}{2\tilde{\beta}_t} \left[ \|\tilde{\boldsymbol{\mu}}_t - \boldsymbol{\mu}_\theta\|^2 \right] \iff \min_{\theta} D_{\text{KL}}(p_\theta(\mathbf{x}_{t-1}|\mathbf{x}_t, \mathbf{y}, d) \parallel q(\mathbf{x}_{t-1}|\mathbf{x}_t, \mathbf{x}_0)). \quad (\text{B6})$$

In other words, minimizing the loss function  $\mathcal{L}_1$  is equivalent to making  $p_\theta(\mathbf{x}_{t-1}|\mathbf{x}_t, \mathbf{y}, d)$  close to  $q(\mathbf{x}_{t-1}|\mathbf{x}_t, \mathbf{x}_0)$ , which completes the proof of the Theorem 2.  $\square$

Further, our final goal is to maximize the likelihood function  $p_\theta(\mathbf{x}_0|\mathbf{y}, d)$  or the log-likelihood  $\log p_\theta(\mathbf{x}_0|\mathbf{y}, d)$  based on the knowledge of VAEs. Then, we give another theorem and the corresponding proof below to show the equivalent relation between the distance of  $p_\theta(\mathbf{x}_{t-1}|\mathbf{x}_t, \mathbf{y}, d)$  and  $q(\mathbf{x}_{t-1}|\mathbf{x}_t, \mathbf{x}_0)$ , and  $\log p_\theta(\mathbf{x}_0|\mathbf{y}, d)$ :

**Theorem 3.** Making  $p_\theta(\mathbf{x}_{t-1}|\mathbf{x}_t, \mathbf{y}, d)$  close to  $q(\mathbf{x}_{t-1}|\mathbf{x}_t, \mathbf{x}_0)$  is equivalent to maximizing the log-likelihood function  $\log p_\theta(\mathbf{x}_0|\mathbf{y}, d)$ .

*Proof.* The proof of this theorem mainly refers to the variational inference in VAEs and [56].

$$\max_{\theta} \log p_\theta(\mathbf{x}_0|\mathbf{y}, d) = \max_{\theta} \log \int_{\mathcal{X}} p_\theta(\mathbf{x}_{0:T}|\mathbf{y}, d) d\mathbf{x}_{1:T}$$

$$\begin{aligned}
 &= \max_{\theta} \log \int_{\mathcal{X}} \frac{p_{\theta}(\mathbf{x}_{0:T}|\mathbf{y}, d)q(\mathbf{x}_{1:T}|\mathbf{x}_0)}{q(\mathbf{x}_{1:T}|\mathbf{x}_0)} d\mathbf{x}_{1:T} \\
 &= \max_{\theta} \log \mathbb{E}_{q(\mathbf{x}_{1:T}|\mathbf{x}_0)} \left[ \frac{p_{\theta}(\mathbf{x}_{0:T}|\mathbf{y}, d)}{q(\mathbf{x}_{1:T}|\mathbf{x}_0)} \right], \tag{B7}
 \end{aligned}$$

where,  $p_{\theta}(\mathbf{x}_{0:T}|\mathbf{y}, d)$  means the joint distribution of  $p_{\theta}(\mathbf{x}_0|\mathbf{y}, d), p_{\theta}(\mathbf{x}_1|\mathbf{y}, d), \dots, p_{\theta}(\mathbf{x}_T|\mathbf{y}, d)$ . Similarly,  $q(\mathbf{x}_{1:T}|\mathbf{x}_0)$  is also the joint distribution. Then, based on the Jensen's inequality, we have

$$\begin{aligned}
 &\max_{\theta} \log p_{\theta}(\mathbf{x}_0|\mathbf{y}, d) \\
 &\geq \max_{\theta} \mathbb{E}_{q(\mathbf{x}_{1:T}|\mathbf{x}_0)} \left[ \log \frac{p_{\theta}(\mathbf{x}_{0:T}|\mathbf{y}, d)}{q(\mathbf{x}_{1:T}|\mathbf{x}_0)} \right] \\
 &= \max_{\theta} \mathbb{E}_{q(\mathbf{x}_{1:T}|\mathbf{x}_0)} \left[ \log \frac{p(\mathbf{x}_T|\mathbf{y}, d) \prod_{t=1}^T p_{\theta}(\mathbf{x}_{t-1}|\mathbf{x}_t, \mathbf{y}, d)}{\prod_{t=1}^T q(\mathbf{x}_t|\mathbf{x}_{t-1})} \right] \\
 &= \max_{\theta} \mathbb{E}_{q(\mathbf{x}_{1:T}|\mathbf{x}_0)} \left[ \log \frac{p(\mathbf{x}_T|\mathbf{y}, d)p_{\theta}(\mathbf{x}_0|\mathbf{x}_1, \mathbf{y}, d)}{q(\mathbf{x}_1|\mathbf{x}_0)} + \log \frac{\prod_{t=2}^T p_{\theta}(\mathbf{x}_{t-1}|\mathbf{x}_t, \mathbf{y}, d)}{\prod_{t=2}^T q(\mathbf{x}_t|\mathbf{x}_{t-1}, \mathbf{x}_0)} \right] \\
 &= \max_{\theta} \mathbb{E}_{q(\mathbf{x}_{1:T}|\mathbf{x}_0)} \left[ \log \frac{p(\mathbf{x}_T|\mathbf{y}, d)p_{\theta}(\mathbf{x}_0|\mathbf{x}_1, \mathbf{y}, d)}{q(\mathbf{x}_T|\mathbf{x}_0)} + \sum_{t=2}^T \log \frac{p_{\theta}(\mathbf{x}_{t-1}|\mathbf{x}_t, \mathbf{y}, d)}{q(\mathbf{x}_{t-1}|\mathbf{x}_t, \mathbf{x}_0)} \right] \\
 &= \max_{\theta} \mathbb{E}_{q(\mathbf{x}_{1:T}|\mathbf{x}_0)} \left[ \log p_{\theta}(\mathbf{x}_0|\mathbf{x}_1, \mathbf{y}, d) + \log \frac{p(\mathbf{x}_T|\mathbf{y}, d)}{q(\mathbf{x}_T|\mathbf{x}_0)} + \sum_{t=2}^T \log \frac{p_{\theta}(\mathbf{x}_{t-1}|\mathbf{x}_t, \mathbf{y}, d)}{q(\mathbf{x}_{t-1}|\mathbf{x}_t, \mathbf{x}_0)} \right] \\
 &= \max_{\theta} \mathbb{E}_{q(\mathbf{x}_1|\mathbf{x}_0)} [\log p_{\theta}(\mathbf{x}_0|\mathbf{x}_1, \mathbf{y}, d)] - \mathbb{E}_{q(\mathbf{x}_T|\mathbf{x}_0)} \left[ \log \frac{q(\mathbf{x}_T|\mathbf{x}_0)}{p(\mathbf{x}_T|\mathbf{y}, d)} \right] - \sum_{t=2}^T \mathbb{E}_{q(\mathbf{x}_{t-1}, \mathbf{x}_t|\mathbf{x}_0)} \left[ \log \frac{q(\mathbf{x}_{t-1}|\mathbf{x}_t, \mathbf{x}_0)}{p_{\theta}(\mathbf{x}_{t-1}|\mathbf{x}_t, \mathbf{y}, d)} \right] \\
 &= \max_{\theta} \left\{ \mathbb{E}_{q(\mathbf{x}_1|\mathbf{x}_0)} [\log p_{\theta}(\mathbf{x}_0|\mathbf{x}_1, \mathbf{y}, d)] - D_{\text{KL}}(q(\mathbf{x}_T|\mathbf{x}_0) \parallel p(\mathbf{x}_T|\mathbf{y}, d)) - \sum_{t=2}^T \mathbb{E}_{q(\mathbf{x}_t|\mathbf{x}_0)} D_{\text{KL}}(q(\mathbf{x}_{t-1}|\mathbf{x}_t, \mathbf{x}_0) \parallel p_{\theta}(\mathbf{x}_{t-1}|\mathbf{x}_t, \mathbf{y}, d)) \right\}, \tag{B8}
 \end{aligned}$$

where  $\mathbb{E}_{q(\mathbf{x}_1|\mathbf{x}_0)} [\log p_{\theta}(\mathbf{x}_0|\mathbf{x}_1, \mathbf{y}, d)]$  is interpreted as a reconstruction term following [56], and DDPM finds that omitting this term is beneficial and doesn't affect the generations.  $D_{\text{KL}}(q(\mathbf{x}_T|\mathbf{x}_0) \parallel p(\mathbf{x}_T|\mathbf{y}, d))$  is a prior matching term. Because  $q(\mathbf{x}_T|\mathbf{x}_0) = \mathcal{N}(\mathbf{x}_T; \sqrt{\bar{\alpha}_T}\mathbf{x}_0, (1 - \bar{\alpha}_T)\mathbf{I}_D)$  (recall Eq. (5)) and when  $T$  closes to infinity,  $q(\mathbf{x}_T|\mathbf{x}_0) \approx \mathcal{N}(\mathbf{x}_T; 0, \mathbf{I}_D)$ , and  $p(\mathbf{x}_T|\mathbf{y}, d) = p(\mathbf{x}_T) = \mathcal{N}(0, \mathbf{I}_D)$  (recall Subsection 4.4), there are no learnable parameters in this term, and this term is approximately equal to 0. Therefore, this matching term can also be omitted.

So,  $\max_{\theta} \log p_{\theta}(\mathbf{x}_0|\mathbf{y}, d) \iff \max_{\theta} - \sum_{t=2}^T \mathbb{E}_{q(\mathbf{x}_t|\mathbf{x}_0)} D_{\text{KL}}(q(\mathbf{x}_{t-1}|\mathbf{x}_t, \mathbf{x}_0) \parallel p_{\theta}(\mathbf{x}_{t-1}|\mathbf{x}_t, \mathbf{y}, d))$

$\iff \min_{\theta} \sum_{t=2}^T \mathbb{E}_{q(\mathbf{x}_t|\mathbf{x}_0)} D_{\text{KL}}(q(\mathbf{x}_{t-1}|\mathbf{x}_t, \mathbf{x}_0) \parallel p_{\theta}(\mathbf{x}_{t-1}|\mathbf{x}_t, \mathbf{y}, d))$ . It is important to note that Eq. (B8) is usually

known as the variational lower bound (VLB) or the evidence lower bound (ELBO) of  $\log p_{\theta}(\mathbf{x}_0|\mathbf{y}, d)$ . By the above derivation, it is clear that maximizing  $\log p_{\theta}(\mathbf{x}_0|\mathbf{y}, d)$  is approximately equivalent to making  $p_{\theta}(\mathbf{x}_{t-1}|\mathbf{x}_t, \mathbf{y}, d)$  close to  $q(\mathbf{x}_{t-1}|\mathbf{x}_t, \mathbf{x}_0)$ . The proof is completed.  $\square$

**Remark 2.** There are two points we should be aware of. (1) Combining Theorem 2 and Theorem 3, we see that minimizing the loss function  $\mathcal{L}_1$  is equivalent to maximize the log-likelihood  $\log p_{\theta}(\mathbf{x}_0|\mathbf{y}, d)$ . Therefore, we prove the effectiveness of the optimization process. (2) In the parameterization of  $p_{\theta}(\mathbf{x}_{t-1}|\mathbf{x}_t, \mathbf{y}, d)$ , we assume that the covariance matrix  $\Sigma_{\theta}(\mathbf{x}_t, t, \mathbf{y}, d)$  is equal to  $\tilde{\Sigma}_t$  that is the covariance matrix of  $q(\mathbf{x}_{t-1}|\mathbf{x}_t, \mathbf{x}_0)$  for simplicity. In fact,  $\Sigma_{\theta}(\mathbf{x}_t, t, \mathbf{y}, d)$  can also be trainable just like  $\mu_{\theta}(\mathbf{x}_t, t, \mathbf{y}, d)$ . We leave that to future work.

## Appendix C Calculation process of the AB

Appendix C details the calculation process of the AB described in Subsection 4.6.3, which consists of a SAB and a PCAB.

**SAB.** It is known that the input tensor is  $\mathbf{M}_s$ . SAB firstly generates Query (**Q**), Key (**K**), and Value (**V**)



matrices by a GN layer, three  $1 \times 1$  convolutions, and reshape operations appended:

$$\mathbf{Q} = \mathbf{R}[\mathbf{W}_Q \times \text{GN}(\mathbf{M}_s)], \quad (\text{C1a})$$

$$\mathbf{K} = \mathbf{R}[\mathbf{W}_K \times \text{GN}(\mathbf{M}_s)], \quad (\text{C1b})$$

$$\mathbf{V} = \mathbf{R}[\mathbf{W}_V \times \text{GN}(\mathbf{M}_s)], \quad (\text{C1c})$$

where  $\mathbf{Q}, \mathbf{K}, \mathbf{V} \in \mathbb{R}^{C \times HW}$ .  $\mathbf{W}_Q, \mathbf{W}_K, \mathbf{W}_V$  represents the Query, Key, and Value weight matrices learned by  $3 \times 3$  convolutions.  $\mathbf{R}$  means the reshape operation. Then self-attention can be computed by the following formula:

$$\text{Attention}(\mathbf{Q}, \mathbf{K}, \mathbf{V}) \triangleq \mathbf{V} \left[ \text{SoftMax} \left( \frac{\mathbf{Q}^T \mathbf{K}}{\sqrt{S}} \right) \right]^T \in \mathbb{R}^{C \times HW}, \quad (\text{C2})$$

where,  $S = C$  represents the scaling parameter to control the magnitude of the product. Finally, the output can be obtained after a skip connection:

$$\mathbf{O}_s = \text{PW Conv}[\mathbf{R}(\text{Attention}(\mathbf{Q}, \mathbf{K}, \mathbf{V}))] + \mathbf{M}_s, \quad (\text{C3})$$

where  $\text{PW Conv}$  is a point-wise convolution. The skip connection is adopted to fuse the original feature.

**PCAB.** The core part of PCAB is the 2 CABs. Because the remaining parts of PCAB have been introduced in [Subsection 4.6.3](#), here we focus on the 2 CABs. Further, since the 2 CABs have the same structures, for simplicity, we just take the  $\text{CAB}(\mathbf{O}_s, \mathbf{E}_t)$  as an example to explain the calculation process of CABs.

Similar with the SAB, CAB also firstly generates Query, Key, and Value matrices:

$$\mathbf{Q} = \mathbf{R}[\mathbf{W}_Q \times \text{GN}(\mathbf{M}_s)], \quad (\text{C4a})$$

$$\mathbf{K}_t = \mathbf{R}[\mathbf{W}_K \times \mathbf{E}_t], \quad (\text{C4b})$$

$$\mathbf{V}_t = \mathbf{R}[\mathbf{W}_V \times \mathbf{E}_t], \quad (\text{C4c})$$

where  $\mathbf{Q} \in \mathbb{R}^{C \times HW}$  and  $\mathbf{W}_Q$  represents the Query projection matrix learned by a  $1 \times 1$  convolution same as the SAB.  $\mathbf{E}_t \in \mathbb{R}^{D_t \times 1 \times 1}$  is an expanded matrix from the vanilla embedding to align with  $\mathbf{M}_s$  on dimensions (the same as the operation in Res-Block).  $\mathbf{W}_K$  and  $\mathbf{W}_V$  represents the Key, and Value projection matrices learned by two point-wise convolutions.  $\mathbf{K}_t, \mathbf{V}_t \in \mathbb{R}^{C \times 1}$ . It is worth noting that this allocation strategy that  $\mathbf{Q}$  comes from  $\mathbf{M}_s$ , and  $\mathbf{K}_t$  and  $\mathbf{V}_t$  come from  $\mathbf{E}_t$  is a common trick when we need to compute cross-attention on data with two kinds of domains, just like Stable Diffusion and Grounding DINO [86] do. Then, plugging  $\mathbf{Q}, \mathbf{K}_t$ , and  $\mathbf{V}_t$  into Eq. (C2) to obtain the  $\text{Attention}(\mathbf{Q}, \mathbf{K}_t, \mathbf{V}_t) \in \mathbb{R}^{C \times HW}$ . Next, the output of  $\text{CAB}(\mathbf{O}_s, \mathbf{E}_t)$  can be finally obtained by executing the following formula:

$$\mathbf{O}_C^t = \text{PW Conv}[\mathbf{R}(\text{Attention}(\mathbf{Q}, \mathbf{K}_t, \mathbf{V}_t))]. \quad (\text{C5})$$

## References

- [1] W. Liao, X. Lu, Y. Huang, Z. Zheng, Y. Lin, Automated structural design of shear wall residential buildings using generative adversarial networks, *Automation in Construction*. 132 (2021), 103931, <https://doi.org/10.1016/j.autcon.2021.103931>.
- [2] X. Lu, W. Liao, Y. Zhang, Y. Huang, Intelligent structural design of shear wall residence using physics-enhanced generative adversarial networks, *Earthquake Engineering & Structural Dynamics*, 51 (2022), pp. 1657-1676, <https://doi.org/10.1002/eqe.3632>.
- [3] P. Zhao, W. Liao, Y. Huang, X. Lu, Intelligent design of shear wall layout based on attention-enhanced generative adversarial network, *Engineering Structures*. 274 (2023), 115170, <https://doi.org/10.1016/j.engstruct.2022.115170>.
- [4] P. Zhao, W. Liao, Y. Huang, X. Lu, Intelligent design of shear wall layout based on graph neural networks, *Advanced Engineering Informatics*. 55 (2023), 101886, <https://doi.org/10.1016/j.aei.2023.101886>.
- [5] Z. He, S. Jiang, J. Zhang, G. Wu, Automatic damage detection using anchor-free method and unmanned surface vessel, *Automation in Construction*. 133 (2022), 104017, <https://doi.org/10.1016/j.autcon.2021.104017>.
- [6] J.K. Chow, Z. Su, J. Wu, P.S. Tan, X. Mao, Y.-H. Wang, Anomaly detection of defects on concrete structures with the

- convolutional autoencoder, *Advanced Engineering Informatics*. 45 (2020), 101105, <https://doi.org/10.1016/j.aei.2020.101105>.
- [7] J.K. Chow, K.-f. Liu, P.S. Tan, Z. Su, J. Wu, Z. Li, Y.-H. Wang, Automated defect inspection of concrete structures, *Automation in Construction*. 132 (2021), 103959, <https://doi.org/10.1016/j.autcon.2021.103959>.
- [8] J. Wei, Y. Tay, R. Bommasani, C. Raffel, B. Zoph, S. Borgeaud, D. Yogatama, M. Bosma, D. Zhou, D. Metzler, E.H. Chi, T. Hashimoto, O. Vinyals, P. Liang, J. Dean, W. Fedus, Emergent abilities of large language models, arXiv:2206.07682v2, <https://arxiv.org/abs/2206.07682>, 2022 (accessed 1 May 2023).
- [9] J. Qian, Z. Zhao, X. Ji, L. Ye, Design of tall building structures. 3rd ed. China Architecture & Building Press; 2018. in Chinese.
- [10] CTBUH, Tall Buildings in 2019: Another Record Year for Supertall Completions, CTBUH Research, 2019. [https://www.skyscrapercenter.com/research/CTBUH\\_ResearchReport\\_2019YearInReview.pdf](https://www.skyscrapercenter.com/research/CTBUH_ResearchReport_2019YearInReview.pdf).
- [11] P.N. Pizarro, L.M. Massone, F.R. Rojas, R.O. Ruiz, Use of convolutional networks in the conceptual structural design of shear wall buildings layout, *Engineering Structures*. 239 (2021), 112311, <https://doi.org/10.1016/j.engstruct.2021.112311>.
- [12] P.N. Pizarro, L.M. Massone, Structural design of reinforced concrete buildings based on deep neural networks, *Engineering Structures*. 241 (2021), 112377, <https://doi.org/10.1016/j.engstruct.2021.112377>.
- [13] Y. Blau, T. Michaeli, The perception-distortion tradeoff, in: 2018 IEEE/CVF Conference on Computer Vision and Pattern Recognition (CVPR), IEEE, Salt Lake City, UT, USA, 2018, pp. 6228-6237, <https://doi.org/10.1109/CVPR.2018.00652>.
- [14] J. Whang, M. Delbracio, H. Talebi, C. Saharia, A. G. Dimakis, P. Milanfar, Deblurring via stochastic refinement, in: 2022 IEEE/CVF Conference on Computer Vision and Pattern Recognition (CVPR), IEEE, New Orleans, LA, USA, 2022, pp. 16272-16282, <https://doi.org/10.1109/CVPR52688.2022.01581>.
- [15] C. Saharia, J. Ho, W. Chan, T. Salimans, D.J. Fleet, M. Norouzi, Image super-resolution via iterative refinement, *IEEE Transactions on Pattern Analysis and Machine Intelligence*. 45 (4) (2023), pp. 4713-4726, <https://doi.org/10.1109/TPAMI.2022.3204461>.
- [16] Z. Chen, Y. Zhang, D. Liu, B. Xia, J. Gu, L. Kong, X. Yuan, Hierarchical integration diffusion model for realistic image deblurring, arXiv:2305.12966v4, <https://arxiv.org/abs/2305.12966>, 2023 (accessed 1 October 2023). Nips
- [17] Z. Wu, S. Pan, F. Chen, G. Long, C. Zhang, P.S. Yu, A Comprehensive Survey on Graph Neural Networks, *IEEE Transactions on Neural Networks and Learning Systems*, 32 (1) (2021), pp. 4-24. <http://doi.org/10.1109/TNNLS.2020.2978386>.
- [18] P. Zhao, Y. Fei, Y. Huang, Y. Feng, W. Liao, X. Lu, Design-condition-informed shear wall layout design based on graph neural networks, *Advanced Engineering Informatics*. 58 (2023), 102190, <https://doi.org/10.1016/j.aei.2023.102190>.
- [19] P. Isola, J.-Y. Zhu, T. Zhou, A.A. Efros, Image-to-Image Translation with Conditional Adversarial Networks, in: 2017 IEEE Conference on Computer Vision and Pattern Recognition (CVPR), IEEE, Honolulu, HI, USA, 2017, pp. 5967-5976, <https://doi.org/10.1109/CVPR.2017.632>.
- [20] D.P. Kingma, M. Welling, Auto-Encoding Variational Bayes, arXiv:1312.6114, <https://arxiv.org/abs/1312.6114>, 2013 (accessed 1 May 2023).
- [21] D.J. Rezende, S. Mohamed, Variational inference with normalizing flows, in: 32nd International Conference on Machine Learning (ICML), PMLR, Lille, France, 2015, pp. 1530-1538, <http://proceedings.mlr.press/v37/rezende15.html>.
- [22] L. Dinh, J. Sohl-Dickstein, S. Bengio, Density estimation using Real NVP, arXiv:1605.08803, <https://arxiv.org/abs/1605.08803>, 2016 (accessed 1 May 2023).
- [23] A. Oord, N. Kalchbrenner, K. Kavukcuoglu, Pixel Recurrent Neural Networks, in: 33rd International Conference on Machine Learning (ICML), PMLR, New York, NY, USA, 2016, pp. 1747-1756, <https://proceedings.mlr.press/v48/oord16.html>.
- [24] I. Goodfellow, J. Pouget-Abadie, M. Mirza, B. Xu, D. Warde-Farley, S. Ozair, A. Courville, Y. Bengio, Generative adversarial nets, *Communications of the ACM*. 63 (11) (2020), pp. 139-144, <https://doi.org/10.1145/3422622>.
- [25] J. Song, C. Meng, S. Ermon, Denoising diffusion implicit models, arXiv: 2010.02502v4, <https://arxiv.org/abs/2010.02502>, 2022 (accessed 20 May 2023).
- [26] T. Karras, S. Laine, T. Aila, A Style-Based Generator Architecture for Generative Adversarial Networks, *IEEE Transactions on Pattern Analysis and Machine Intelligence*. 43 (12) (2021), pp. 4217-4228, <https://doi.org/10.1109/TPAMI.2020.2970919>.

- [27] O. Kupyn, V. Budzan, M. Mykhailych, D. Mishkin, J. Matas, DeblurGAN: Blind motion deblurring using conditional adversarial networks, in: 2018 IEEE/CVF Conference on Computer Vision and Pattern Recognition (CVPR), IEEE, Salt Lake City, UT, USA, 2018, pp. 8183-8192, <https://doi.org/10.1109/CVPR.2018.00854>.
- [28] C. Ledig, L. Theis, F. Huszár, J. Caballero, A. Cunningham, A. Acosta, A. Aitken, A. Tejani, J. Totz, Z. Wang, W. Shi, Photo-realistic single image super-resolution using a generative adversarial network, in: 2017 IEEE Conference on Computer Vision and Pattern Recognition (CVPR), IEEE, Honolulu, HI, USA, 2017, pp. 105-114, <https://doi.org/10.1109/CVPR.2017.19>.
- [29] S. Jiang, J. Zhang, W. Wang, Y. Wang, Automatic Inspection of Bridge Bolts Using Unmanned Aerial Vision and Adaptive Scale Unification-Based Deep Learning, *Remote Sensing*, 15 (2) 2023, 328, <https://doi.org/10.3390/rs15020328>.
- [30] F. Ni, Z. He, S. Jiang, W. Wang, J. Zhang, A Generative adversarial learning strategy for enhanced lightweight crack delineation networks, *Advanced Engineering Informatics*, 52 (2022), 101575, <https://doi.org/10.1016/j.aei.2022.101575>.
- [31] T. Jin, X.W. Ye, Z.X. Li, Establishment and evaluation of conditional GAN-based image dataset for semantic segmentation of structural cracks, *Engineering Structures*, 285 (2023), 116058, <https://doi.org/10.1016/j.engstruct.2023.116058>.
- [32] N. Nauata, K.-H. Chang, C.-Y. Cheng, G. Mori, Y. Furukawa, House-GAN: Relational Generative Adversarial Networks for Graph-Constrained House Layout Generation, in: 2020 European Conference on Computer Vision (ECCV), Springer, Glasgow, UK, 2020, pp. 162-177, [https://doi.org/10.1007/978-3-030-58452-8\\_10](https://doi.org/10.1007/978-3-030-58452-8_10).
- [33] N. Nauata; S. Hosseini; K.-H. Chang; H. Chu; C.-Y. Cheng; Y. Furukawa, House-GAN++: Generative Adversarial Layout Refinement Network towards Intelligent Computational Agent for Professional Architects, in: 2021 IEEE/CVF Conference on Computer Vision and Pattern Recognition (CVPR), IEEE, Nashville, TN, USA, 2021, pp. 13627-13636, <https://doi.org/10.1109/CVPR46437.2021.01342>.
- [34] F. He, Y. Huang, H. Wang, iPLAN: Interactive and Procedural Layout Planning, in: 2022 IEEE/CVF Conference on Computer Vision and Pattern Recognition (CVPR), IEEE, New Orleans, LA, USA, 2022, pp. 7783-7792, <https://doi.org/10.1109/CVPR52688.2022.00764>.
- [35] X. Liu, X. Wang, G. Wright, J.C.P. Cheng, X. Li, R. Liu, A State-of-the-Art Review on the Integration of Building Information Modeling (BIM) and Geographic Information System (GIS), *ISPRS International Journal of Geo-Information*. 6 (2) (2017), 53, <https://doi.org/10.3390/ijgi6020053>.
- [36] Technical Circular (Works), Adoption of Building Information Modelling for Capital Works Projects in Hong Kong, Development Bureau of Hong Kong SAR, 2021.
- [37] M. Arjovsky, S. Chintala, L. Bottou, Wasserstein generative adversarial networks, in: 34th International Conference on Machine Learning (ICML), PMLR, Sydney, Australia, 2017, pp. 214-223, <https://proceedings.mlr.press/v70/arjovsky17a.html>.
- [38] T.C. Wang, M.Y. Liu, J.Y. Zhu, A. Tao, J. Kautz, B. Catanzaro, High-resolution image synthesis and semantic manipulation with conditional GANs, in: 2018 IEEE/CVF Conference on Computer Vision and Pattern Recognition (CVPR), IEEE, Salt Lake City, UT, USA, 2018, pp. 8798-8807, <https://doi.org/10.1109/CVPR.2018.00917>.
- [39] L. Metz, B. Poole, D. Pfau, J. Sohl-Dickstein, Unrolled Generative Adversarial Networks, in: 2017 International Conference on Learning Representations (ICLR), Toulon, France, 2017, pp.1-25, <https://openreview.net/forum?id=BydrOIcIc>.
- [40] A. Srivastava, L. Valkov, C. Russell, M.U. Gutmann, C. Sutton, VEEGAN: Reducing mode collapse in GANs using implicit variational learning, in: 2017 International Conference on Neural Information Processing Systems (NIPS), ACM, Long Beach, CA, USA, 2017, pp. 3310-3320, <https://dl.acm.org/doi/10.5555/3294996.3295090>.
- [41] J. Sohl-Dickstein, E. Weiss, N. Maheswaranathan, S. Ganguli, Deep unsupervised learning using nonequilibrium thermodynamics, in: 32nd International Conference on Machine Learning (ICML), PMLR, Lille, France, 2015, pp. 2256-2265, <https://proceedings.mlr.press/v37/sohl-dickstein15.html>.
- [42] J. Ho, A. Jain, P. Abbeel, Denoising diffusion probabilistic models, in: 34th International Conference on Neural Information Processing Systems (NeurIPS), ACM, Vancouver, BC, Canada, 2020, pp. 6840-6851, <https://dl.acm.org/doi/abs/10.5555/3495724.3496298>.
- [43] P. Dhariwal, A. Nichol, Diffusion models beat gans on image synthesis, in: 35th International Conference on Neural Information

- Processing Systems (NeurIPS), Curran Associates, Inc, Online, 2021, pp. 8780-8794, <https://proceedings.neurips.cc/paper/2021/hash/49ad23d1ec9fa4bd8d77d02681df5cfa-Abstract.html>.
- [44] R. Rombach, A. Blattmann, D. Lorenz, P. Esser, B. Ommer, High-resolution image synthesis with latent diffusion models, in: 2022 IEEE/CVF Conference on Computer Vision and Pattern Recognition (CVPR), IEEE, New Orleans, LA, USA, 2022, pp. 10674-10685, <https://doi.org/10.1109/CVPR52688.2022.01042>.
- [45] B. Kawar, M. Elad, S. Ermon, J. Song, Denoising diffusion restoration models, in: 36th International Conference on Neural Information Processing Systems (NeurIPS), Curran Associates, Inc, New Orleans, USA, 2022, pp. 23593-23606, [https://proceedings.neurips.cc/paper\\_files/paper/2022/hash/95504595b6169131b6ed6cd72eb05616-Abstract-Conference.html](https://proceedings.neurips.cc/paper_files/paper/2022/hash/95504595b6169131b6ed6cd72eb05616-Abstract-Conference.html).
- [46] Y. Wang, J. Yu, J. Zhang, Zero-shot image restoration using denoising diffusion null-space model, in: 2023 International Conference on Learning Representations (ICLR), Kigali Rwanda, 2023, pp. 1-31, <https://openreview.net/forum?id=mRieQgMtNTQ>.
- [47] Z. Luo, F.K. Gustafsson, Z. Zhao, J. Sjölund, T.B. Schön, Image restoration with mean-reverting stochastic differential equations, in: 40th International Conference on Machine Learning (ICML), PMLR, Honolulu, HI, USA, 2023.
- [48] X.-J. Li, J.-Y. Lai, C.-Y. Ma, C. Wang, Using BIM to research carbon footprint during the materialization phase of prefabricated concrete buildings: A China study, *Journal of Cleaner Production*. 279 (2021), 123454, <https://doi.org/10.1016/j.jclepro.2020.123454>.
- [49] V.J.L. Gan, M. Deng, K.T. Tse, C.M. Chan, I.M.C. Lo, J.C.P. Cheng, Holistic BIM framework for sustainable low carbon design of high-rise buildings, *Journal of Cleaner Production*. 195 (2018), pp. 1091-1104, <https://doi.org/10.1016/j.jclepro.2018.05.272>.
- [50] Y. Xu, X. Tao, M. Das, H.H.L. Kwok, H. Liu, G. Wang, J.C.P. Cheng, Suitability analysis of consensus protocols for blockchain-based applications in the construction industry, *Automation in Construction*. 145 (2023), 104638, <https://doi.org/10.1016/j.autcon.2022.104638>.
- [51] W.Y. Chau, Y.-H. Wang, S.W. Chiu, P.S. Tan, M.L. Leung, H.L. Lui, J. Wu, Y.M. Lau, AI-IoT integrated framework for tree tilt monitoring: A case study on tree failure in Hong Kong, *Agricultural and Forest Meteorology*. 341 (2023), 109678, <https://doi.org/10.1016/j.agrformet.2023.109678>.
- [52] D.J. Scott, T. Broyd, L. Ma, Exploratory literature review of blockchain in the construction industry, *Automation in Construction*. 132 (2021), 103914, <https://doi.org/10.1016/j.autcon.2021.103914>.
- [53] Z. Chen, K. Chen, C. Song, X. Zhang, J.C.P. Cheng, Dezhi Li, Global path planning based on BIM and physics engine for UGVs in indoor environments, *Automation in Construction*. 139 (2022), 104263, <https://doi.org/10.1016/j.autcon.2022.104263>.
- [54] C. Zhang, F. Wang, Y. Zou, J. Dimyadi, B.H.W. Guo, L. Hou, Automated UAV image-to-BIM registration for building façade inspection using improved generalised Hough transform, *Automation in Construction*. 153 (2023), 104957, <https://doi.org/10.1016/j.autcon.2023.104957>.
- [55] J. Chen, W. Lu, Y. Fu, Z. Dong, Automated facility inspection using robotics and BIM: A knowledge-driven approach, *Advanced Engineering Informatics*. 55 (2023), 101838, <https://doi.org/10.1016/j.aei.2022.101838>.
- [56] C. Luo, Understanding Diffusion Models: A Unified Perspective, arXiv:2208.11970v1, <https://arxiv.org/abs/2208.11970>, 2022 (accessed 1 May 2023).
- [57] GB 50002–2021, General Code for Seismic Precaution of Buildings and Municipal Engineering, China Architecture & Building Press, Beijing, 2021 in Chinese.
- [58] GB 50011–2010, Code for Seismic Design of Buildings, China Architecture & Building Press, Beijing, 2016 in Chinese.
- [59] L. Weng, What are diffusion models? Lil'Log. <https://lilianweng.github.io/posts/2021-07-11-diffusion-models>, 2022 (accessed 1 May 2023).
- [60] A. Nichol, P. Dhariwal, Improved denoising diffusion probabilistic models, in: 38th International Conference on Machine Learning (ICML), PMLR, Online, 2021, pp. 8162-8171, <https://proceedings.mlr.press/v139/nichol21a.html>.
- [61] JGJ3–2010, Technical Specification for Concrete Structures of Tall Building, China Architecture & Building Press, Beijing, 2010 in Chinese.

- [62] L. Huang, D. Chen, Y. Liu, Y. Shen, D. Zhao, J. Zhou, Composer: Creative and controllable image synthesis with composable conditions, arXiv:2302.09778v2, <https://arxiv.org/abs/2302.09778>, 2023 (accessed 1 June 2023).
- [63] X. Ju, A. Zeng, C. Zhao, J. Wang, L. Zhang, Q. Xu, HumanSD: A native skeleton-guided diffusion model for human image generation, arXiv:2304.04269v1, <https://arxiv.org/abs/2304.04269>, 2023 (accessed 1 June 2023).
- [64] A. Vaswani, N. Shazeer, N. Parmar, J. Uszkoreit, L. Jones, A.N. Gomez, et al., Attention is all you need, in: 2017 International Conference on Neural Information Processing Systems (NIPS), ACM, Long Beach, CA, USA, 2017, pp. 6000-6010, <https://dl.acm.org/doi/10.5555/3295222.3295349>.
- [65] O. Ronneberger, P. Fischer, T. Brox, U-Net: Convolutional networks for biomedical image segmentation, in: 2015 International Conference on Medical Image Computing and Computer-Assisted Intervention (MICCAI), Springer, Munich, Germany, 2015, pp. 234-241, [https://doi.org/10.1007/978-3-319-24574-4\\_28](https://doi.org/10.1007/978-3-319-24574-4_28).
- [66] W. Chen, Z. He, J. Zhang, Online monitoring of crack dynamic development using attention-based deep networks, *Automation in Construction*. 154 (2023), 105022, <https://doi.org/10.1016/j.autcon.2023.105022>.
- [67] W. Peebles, S. Xie, Scalable Diffusion Models with Transformers, arXiv:2212.09748v2, <https://arxiv.org/abs/2212.09748>, 2023 (accessed 1 June 2023). ICCV 2023.
- [68] S. Elfving, E. Uchibe, K. Doya, Sigmoid-weighted linear units for neural network function approximation in reinforcement learning, *Neural Networks*. 107 (2018), pp. 3-11, <https://doi.org/10.1016/j.neunet.2017.12.012>.
- [69] K. He, X. Zhang, S. Ren, J. Sun, Deep residual learning for image recognition, in: 2016 IEEE Conference on Computer Vision and Pattern Recognition (CVPR), IEEE, Las Vegas, NV, USA, 2016, pp. 770-778, <https://doi.org/10.1109/CVPR.2016.90>.
- [70] Z. He, W. Cheng, J. Zhang, Y.-H. Wang, Infrastructure crack segmentation: Boundary guidance method and benchmark dataset, arXiv: 2306.09196v1, <https://arxiv.org/abs/2306.09196>, 2023 (accessed 23 July 2023).
- [71] A. Dosovitskiy, L. Beyer, A. Kolesnikov, D. Weissenborn, X. Zhai, T. Unterthiner, et al., An image is worth 16x16 words: Transformers for image recognition at scale, in: 2021 International Conference on Learning Representations (ICLR), Online, 2021, pp.1-21, <https://openreview.net/forum?id=YicbFdNTTy>.
- [72] S. Zhao, F. Kang, J. Li, Concrete dam damage detection and localisation based on YOLOv5s-HSC and photogrammetric 3D reconstruction, *Automation in Construction*. 143 (2022), 104555, <https://doi.org/10.1016/j.autcon.2022.104555>.
- [73] Y. Lu, W. Qin, C. Zhou, Z. Liu, Automated detection of dangerous work zone for crawler crane guided by UAV images via Swin Transformer, *Automation in Construction*. 147 (2023), 104744, <https://doi.org/10.1016/j.autcon.2023.104744>.
- [74] J. Chen, Y. Lu, Q. Yu, X. Luo, E. Adeli, Y. Wang, TransUNet: Transformers make strong encoders for medical image segmentation, arXiv:2102.04306v1, <https://arxiv.org/abs/2102.04306>, 2021 (accessed 1 October 2022).
- [75] W. Yu, K. Yang, H. Yao, X. Sun, P. Xu, Exploiting the complementary strengths of multi-layer CNN features for image retrieval, *Neurocomputing*. 237 (2017), pp. 235-241, <http://dx.doi.org/10.1016/j.neucom.2016.12.002>.
- [76] Wenjie-liao, StructGAN\_v1, Github. [https://github.com/wenjie-liao/StructGAN\\_v1](https://github.com/wenjie-liao/StructGAN_v1), 2020 (accessed 1 Dec 2022).
- [77] T. Salimans, I. Goodfellow, W. Zaremba, V. Cheung, A. Radford, X. Chen, Improved techniques for training GANs, in: 2016 International Conference on Neural Information Processing Systems (NIPS), ACM, Barcelona, Spain, 2016, pp. 2234-2242, <https://dl.acm.org/doi/10.5555/3157096.3157346>.
- [78] M. Heusel, H. Ramsauer, T. Unterthiner, B. Nessler, S. Hochreiter, GANs trained by a two time-scale update rule converge to a local nash equilibrium, in: 2017 International Conference on Neural Information Processing Systems (NIPS), ACM, Long Beach, CA, USA, 2017, pp. 6629-6640, <https://dl.acm.org/doi/10.5555/3295222.3295408>.
- [79] W. Liao, Y. Huang, Z. Zheng, X. Lu, Intelligent generative structural design method for shear wall building based on “fused-text-image-to-image” generative adversarial networks, *Expert Systems with Applications*. 210 (2022), 118530, <https://doi.org/10.1016/j.eswa.2022.118530>.
- [80] M. Lucic, K. Kurach, M. Michalski, O. Bousquet, S. Gelly, Are GANs created equal? A large-scale study, in: 2018 International Conference on Neural Information Processing Systems (NIPS), ACM, Montréal, Canada, 2018, pp. 698-707, <https://dl.acm.org/doi/10.5555/3326943.3327008>.
- [81] C. Szegedy, V. Vanhoucke, S. Ioffe, J. Shlens, Z. Wojna, Rethinking the inception architecture for computer vision, in: 2016 IEEE

- Conference on Computer Vision and Pattern Recognition (CVPR), IEEE, Las Vegas, NV, USA, 2016, pp. 1063-6919, <https://doi.org/10.1109/CVPR.2016.308>.
- [82] Mseitzer, FID score for PyTorch, Github. <https://github.com/mseitzer/pytorch-fid>, 2020 (accessed 1 August 2023).
- [83] Yang Song, Stefano Ermon, Generative Modeling by Estimating Gradients of the Data Distribution, in: 33rd International Conference on Neural Information Processing Systems (NeurIPS), ACM, Vancouver, BC, Canada, 2019, pp. 11918-11930, <https://dl.acm.org/doi/abs/10.5555/3454287.3455354>.
- [84] Yang Song, Jascha Sohl-Dickstein, Diederik P Kingma, Abhishek Kumar, Stefano Ermon, Ben Poole, Score-Based Generative Modeling through Stochastic Differential Equations, in: 2021 International Conference on Learning Representations (ICLR), Online, 2021, pp.1-36, <https://openreview.net/forum?id=PXTIG12RRHS>.
- [85] K. P. Murphy, Probabilistic Machine Learning: An Introduction, MIT Press, <https://mitpress.mit.edu/9780262046824/probabilistic-machine-learning>, 2022.
- [86] S. Liu, Z. Zeng, T. Ren, F. Li, H. Zhang, J. Yang, C. Li, J. Yang, H. Su, J. Zhu, L. Zhang, Grounding DINO: Marrying DINO with grounded pre-training for open-set object detection, arXiv: 2303.05499v4, <https://arxiv.org/abs/2303.05499>, 2023 (accessed 23 July 2023).